The Astrophysical Journal, 961:105 (16pp), 2024 January 20 https://doi.org/10.3847/1538-4357/acfa9c

Formation of Massive Black Holes with $M = (10^3–10^8)\ M_\odot$ at Pre-quasar Epochs through Hoyle–Lyttleton–Bondi Accretion of Self-interacting Dark Matter onto a Moving Seed

Nirmali Das and Sanjeev Kalita
Department of Physics, Gauhati University, Jalukbari, Guwahati 781014, Assam, India
Received 2022 July 27; revised 2023 August 31; accepted 2023 September 15; published 2024 January 17

Abstract

The presence of supermassive black holes with $M \sim 10^9\ M_\odot$ hosted by the luminous quasars at cosmological redshift $z \geqslant 6$ is still an open problem in astrophysical cosmology. Here we study the formation of massive black holes at high redshift ($z \gg 7$) through Hoyle–Lyttleton–Bondi accretion of self-interacting dark matter (SIDM) onto a 20 $M_\odot$ seed black hole moving with a velocity $\sim$100 km s^{-1} inside the short, mean-free path region of an SIDM halo. We consider observational constraints on a specific SIDM cross section, $\sigma/m_{\rm dm} = (0.1–5)\ {\rm cm^2\ g^{-1}}$. Formation timescale of massive black holes with $M = (10^3–10^8)\ M_\odot$ is calculated for the universal Navarro–Frenk–White (NFW) profile, singular isothermal sphere (SIS), other power-law profiles with a cusp index $2.19 \leqslant \gamma \leqslant 2.5$ of accreted dark matter, and modified-core isothermal profiles. The ambient sound speed is taken as $C_s = (10–100)$ km s^{-1}. It is found that an NFW profile with halo concentration $C = 4.75–32.58$ estimated at $z = 20$ and 30 for halo masses $M_{200} = (10^{12}–10^{14})\ M_\odot$ favors formation of massive black holes with $M = (10^3–10^8)\ M_\odot$ at high redshift, well before quasar epoch. In this profile, these black holes grow within timescales (0.1–69) Myr at $z = 16–20$. For the SIS profile, the black hole formation timescales are short compared to NFW. For power-law profiles, massive black holes with $M = (10^6–10^8)\ M_\odot$ grow within a few tens to 100 Myr ($z = 5–30$). For modified-core isothermal profiles, the timescale of massive black hole formation is in the range (0.79–464.08) Myr ($z = 8–30$).

Unified Astronomy Thesaurus concepts: Supermassive black holes (1663); Dark matter (353); Bondi accretion (174)

1. Introduction

After half a century since the first proposal of existence of a massive black hole at the center of the Galaxy (Lynden-Bell & Rees 1971), the mechanism of formation of the supermassive black hole (SMBH) at the Galactic center and of others that populate the center of external galaxies is still poorly understood. Discovery of very high-redshift quasars, powered by massive black holes, makes the puzzle deeper—how do such massive black holes grow in the infancy of the Universe? Observations of SMBHs with mass $M \sim 10^9\ M_\odot$ within high-redshift quasars at $z \sim 6–7$, corresponding to about 800 Myr after the Big Bang, are extremely puzzling and are well recognized as a fundamental problem of astrophysical cosmology.

A generally accepted idea is the existence of heavy-seed black holes in the early Universe that grew into SMBHs by gas accretion (Begelman et al. 2006). In the simple Eddington accretion model, a seed mass $M_{\rm seed}$ grows to a black hole mass $M_{\rm BH}$ within time Δt according to the relation $M_{\rm BH} = M_{\rm seed}\ \exp(\Delta\ t/\tau)$, where $\tau \sim (450/f_{\rm Edd})(\epsilon/(1–\epsilon))$ (Feng et al. 2021) with $\epsilon \sim 0.1$ being radiation efficiency and $f_{\rm Edd}$ being accretion efficiency. The accretion efficiency is defined as $f_{\rm Edd} = L_{\rm bol}/L_{\rm Edd}$ with $L_{\rm bol}$ being the observed bolometric luminosity and $L_{\rm Edd} \sim 10^{38}$ erg s^{-1} $M\ M_\odot^{-1}$ being Eddington luminosity. Critical accretion $f_{\rm Edd} = 1$ can generate $M_{\rm BH} \sim 10^9\ M_\odot$ for a seed of about $10^4\ M_\odot$ within $\Delta t = 597$ Myr ($z = 30–7.51$) for the quasar J1007+2115 at $z = 7.51$. It is possible to get such seeds through direct collapse of primordial gas clumps (Begelman et al. 2006). But observation of subcritical accretion $f_{\rm Edd} \sim 0.16$ for the quasar J1205-0000 with $M_{\rm BH} = 2.2 \times 10^9\ M_\odot$ at $z = 6.7$ requires a seed of about $10^8\ M_\odot$. It is difficult to achieve such great mass through direct collapse.

Several SMBHs powering quasars have been found at high redshift. Massive black holes with $M = (10^8–10^{10})\ M_\odot$ have been reported (Wu et al. 2015; Banados et al. 2018; Matsuoka et al. 2019; Wang et al. 2021). These black holes formed within only 920 million yr of the Big Bang. Near-infrared spectra of 37 QSOs in the redshift range $6.3 < z \leqslant 7.64$, including 32 QSOs in $z > 6.5$, taken with Keck, Gemini, and Magellan Telescopes and the Very Large Telescope, have shown that central black hole masses (derived from Mg II emission lines) are in the range $(0.3–3.6) \times 10^9\ M_\odot$, which requires seeds as massive as $(10^3–10^4)\ M_\odot$, assuming Eddington rate of accretion since the epoch of $z = 30$. Formation of $M = (10^5–10^6)\ M_\odot$ black holes through direct collapse in atomic cooling halos with virial temperature of $T > 10^4$ K has been discussed by Latif et al. (2013). A quasar at redshift $z = 7.64$ hosts a black hole of mass $1.3 \times 10^9\ M_\odot$ (J0313-1806) (Wang et al. 2021). Another quasar at $z = 7.085$ seems to be powered by a black hole of mass $2 \times 10^9\ M_\odot$ (Mortlock et al. 2011), which leaves only 800 Myr for the growth of the latter. Recently, the CEERS team of the James Webb Space Telescope (JWST) has identified a $10^7\ M_\odot$ black hole in a galaxy at $z = 8.679$ (Larson et al. 2023). One of the generally acclaimed possibilities is that these black holes are the results of growth by accretion of environmental gas onto massive seeds of intermediate masses (Mortlock et al. 2011). The Population III stars and supermassive stars (SMSs) could play the role of progenitors for such seeds in the early Universe. The general cosmogenic picture is that these first massive stars could form around $z = 10–20$ inside dark matter halos that formed within $z = 20–30$ (Haiman et al. 1997). Formation of

Table 1
Mechanisms of Formation of Massive Black Holes Available in the Literature

Available Mechanisms for Formation of Seeds	References
Collapse of single very massive or supermassive stars	Begelman et al. (2006)
Runaway stellar mergers in young dense clusters	Reinoso et al. (2018)
Hierarchical black hole mergers	Giersz et al. (2015)
Intersection and collapse of cosmic string loops	Hawking (1989)
Gravothermal collapse of SIDM	Carr & Kuhnel (2020)

seeds from SMSs ($M \sim(10^4$–$10^6)\ M_\odot$) at $z \geqslant 10$ (Bromm & Loeb 2003) has also been studied. In addition to this mostly studied mechanism, recent years have seen the advent of alternatives for accommodating massive black hole seeds at high redshift through the core collapse of self-interacting dark matter (SIDM; Feng et al. 2021) halos.

The mechanism of formation of the SMBHs provides a link between stellar-mass black holes or the black holes found in the LIGO–Virgo mass spectrum and these objects via intermediate mass black holes (IMBHs) with $M \sim(10^3$–$10^5)\ M_\odot$. There are several mechanisms to accommodate the existence of massive seeds that grow to SMBHs. Many of these mechanisms are based on the seminal idea put by Rees (1978; see Volonteri et al. 2021), which described growth of these black holes from primordial gas clouds. These mechanisms involving seeds with mass range $M = (10^2$–$10^6)\ M_\odot$ have been extensively reviewed in Volonteri et al. (2021).

In a 2019 white paper for the Astro2020 Decadal Survey, Pacucci et al. (2019) emphasized the possibility of formation of SMBHs from direct-collapse black holes acting as seeds in the high-redshift Universe. These are heavy-seed black holes formed by direct gravitational collapse of primordial gas clouds in high-temperature environments near active star-forming protogalaxies (Haehnelt & Rees 1993; Bromm & Loeb 2003; Lodato & Natarajan 2006). They are expected to lead to seeds with mass range $M = (10^4$–$10^6)\ M_\odot$. The white paper discussed the possibility of detecting these heavy seeds by future observing missions such as the JWST, Athena, and the proposed Lynx mission. Here we investigate a competitive mechanism to generate such heavy seeds through dark matter accretion. Mechanisms of growth of SMBHs recently being exercised are summarized in Table 1.

Formation of these SMBHs also impinges upon cosmology. It requires consideration of the cosmogony involving cold dark matter (CDM). The basic mechanism of cosmic structure formation is as follows. Baryons fall gravitationally and cool inside CDM halos that grew from primordial density contrasts. These density contrasts were generated by quantum fluctuations during the cosmic inflation (Springel et al. 2006). When baryons became sufficiently cold and dense inside the CDM halos, star formation was ignited and galaxies formed. Higher overdensities of baryons led to formation of massive galaxies where seed black holes grew by some unknown processes. These seeds then grew to SMBHs (Volonteri et al. 2021). Formation of seed black holes from primordial black holes resulting from phase transitions in the very early Universe is also a possibility.

The role of dark matter in the formation of SMBHs is a new avenue. The origin of SMBHs in the high-redshift Universe through gravothermal collapse of SIDM has been studied earlier (Feng et al. 2021; see Section 1.1). SIDM has a natural mechanism to erase some small-scale problems of the standard CDM paradigm (core-cusp problem; Moore 1994; Moore et al. 1999; De Blok 2010; Tulin & Yu 2017). Recent studies have shown that SIDM is eligible to generate several dark matter distributions in galactic scales (Vogelsberger et al. 2014; Tulin & Yu 2017). SIDM and associated physical processes leading to galactic cores and mass distribution are parameterized by the ratio of self-interacting cross section to the mass of the dark matter particles ($\sigma/m_{\rm dm}$). Earlier, Balberg & Shapiro (2002) discussed formation of massive black holes through gravothermal collapse of only SIDM. But Feng et al. (2021) added baryons in the picture and found that core-collapse timescales are significantly reduced relative to the Hubble time.

The idea of the collapse of fermionic dark matter onto massive black holes has recently appeared. That purely fermionic dark matter core collapses to massive black holes beyond a critical limit of mass has been recently proposed by Arguelles (2021). It requires core-halo configurations where the fermionic dark matter core collapses to SMBH for $M > M_{\rm critical} \sim 10^9\ M_\odot$ with dark matter particles carrying mass within the keV range.

Gravothermal collapse of dark matter has been realized as a serious alternative for explaining the formation of high-redshift massive black holes (Balberg & Shapiro 2002; Feng et al. 2021). If dark matter collapses to form black holes, it must be self-interacting. Recently, Misner (2023) conjectured that dark matter may have sufficient self-interactions at $z = 1000$–$(20$–$7)$ (the lower redshifts being accessible to JWST), leading to sufficient pressure and viscosity. This may generate sufficient SIDM to lead to the generation of SMBHs. That SIDM halo collapses to form seed black holes through gravothermal collapse is a well-studied problem (Balberg & Shapiro 2002; Balberg et al. 2002; Feng et al. 2021). Gravothermal collapse refers to the collapse of self-gravitating systems due to negative specific heat (Binney & Tremaine 1987), and it was first studied in gravitating systems in Lynden-Bell & Wood (1968) and Lynden-Bell & Eggelton (1980). It proceeds as follows. Slight contraction of the halo core increases its temperature and transfers heat to the outer halo through mass loss or conduction (exactly like collapse of a globular cluster due to star ejection through self-gravitational scattering). If the magnitude of the heat capacity of the outer halo is less than that of the core, the halo temperature soon rises above the temperature of the core, and the heat flow stops. However, if the heat capacity of the halo is far above that of the core, the thermal inertia of the outer halo causes continuous loss of mass from the core. Dark matter evaporation continues, and the core keeps on contracting. In this regime, the mean-free path of collision between dark matter particles ($\lambda = \left(\frac{1}{\rho}\right)\left(\frac{\sigma}{m_{dm}}\right)^{-1}$, with ρ being ambient density and $\sigma/m_{\rm dm}$ being self-interacting cross section per unit of dark matter particle mass) remains larger than the gravitational scale height ($H = v/\sqrt{4\pi G\rho}$, v being the velocity dispersion in the halo) ($\lambda > H$) of the system (Balberg et al. 2002). This gravothermal collapse continues until the transition regime $\lambda \sim H$. Past this point, the core becomes so dense that the mean-free path of dark matter collision become smaller than the scale height ($\lambda < H$; Balberg & Shapiro 2002). The system thus bifurcates into small mean-free path (SMFP; larger cross section) and large mean-free path (LMFP; small cross section or weakly collisional). In the SMFP regime, the core becomes

dense enough to ignite dynamical instability, leading to the formation of a massive black hole precursor. However, the entire SMFP core does not undergo collapse to form a black hole; rather, a tiny fraction of it undergoes dynamical instability (see Section 3.2). This black hole then Bondi accretes the surrounding dark matter to grow into a massive black hole.

In this work, we attempt to study the spherical accretion of SIDM onto some initial seed. We follow the method adopted by Ostriker (2000). This is the method of Bondi accretion. Can we generate the seeds through dark matter accretion within a few hundred million years? In Section 2, we present the formation mechanism of seeds by considering the Hoyle–Lyttleton–Bondi (HLB) accretion with the saturation condition that the outer accretion radius is equal to the mean-free path of collisional dark matter particles and thereby estimate the core mass formed by taking available observational bounds on cross section per unit mass of the SIDM. In Section 3, we study the growth of (10^3–10^8) $M_\odot$ black holes from a 20 $M_\odot$ seed with the Navarro–Frenk–White (NFW) profile, SIS, power profiles with cusp index $2.19 \leqslant \gamma \leqslant 2.5$, and two modified-core isothermal profiles inside an SMFP core and explore the nature and mass of the SMFP core and stability of the seed inside the dark matter halo. In Section 4, we study the timescales of the formation of the massive black holes of mass (10^3–10^8) $M_\odot$ in the NFW profile, singular isothermal sphere (SIS), power profiles of dark matter, and modified-core isothermal profiles and estimate the corresponding cosmological redshifts. Section 5 presents the results and discussion. Section 6 concludes with future prospects of the findings.

2. Hoyle–Lyttleton–Bondi Model

Ostriker (2000) analyzed the possibility of the formation of massive black holes through accretion of collisional dark matter onto seed black holes of about 25 $M_\odot$, which are usually assumed to be remnants of 100 $M_\odot$ Population III stars. Considerations of the high-redshift black hole mass function also indicate a population of stellar-mass black holes of a few tens of solar masses (see Section 3). This is quasi-spherical accretion rather than accretion in the form of a rotationally supported disk, which is the case of normal baryonic matter where electromagnetic radiative losses are efficient. But in the case of nondissipative dark matter, the radiative loss is negligible, and hence, matter gets accreted with nearly spherical shape. In this case, radiation pressure cannot prevent the accretion rate from being supercritical.

The accretion rate is expressed by the HLB model (Bondi & Hoyle 1944) where $M_{\rm BH}$ accepts the infalling mass at a higher rate and therefore grows more rapidly than allowed by the Eddington rate. The accretion rate depends on the surrounding density of the dark matter fluid ρ_s and sound speed in the fluid, $C_{\rm s} = \sqrt{\frac{\partial p}{\partial \rho}}$, and it is given as

$$\dot{M}_{\rm BH} = 4\pi r_A^2 C_s \rho_s, \tag{1}$$

where $r_A = \frac{GM_{\rm BH}}{C_s^2}$ is the outer accretion radius (Bondi 1947).

Therefore,

$$\dot{M}_{\rm BH} = \frac{4\pi G^2 M_{\rm BH}^2 \rho_s}{C_s^3}. \tag{2}$$

In general, the HLB model treats accretion onto a compact object moving with velocity v supersonically in an otherwise homogeneous medium, and the accretion rate is expressed as (Bondi 1952; Cruz-Osorio et al. 2017)

$$\dot{M}_{\rm BH} = \frac{4\pi G^2 M_{\rm BH}^2 \rho_s}{(v_s^2 + C_s^2)^{\frac{3}{2}}}, \tag{3}$$

where ρ_s is the density of the otherwise homogeneous medium. This is a guiding principle for estimating accretion rate in compact stars in binaries (Petterson 1978) or in estimating gas supply to central SMBHs in cosmological simulations (Springel et al. 2005; Blecha et al. 2013). Relativistic HLB accretion in presence of small obstacles around the accreting compact object has been studied by Cruz-Osorio et al. (2017). This study has been found to carry prospects for understanding the growth of primordial black holes in the radiation era (Lora-Clavijo et al. 2013; Penner 2013).

This growth (Equation (2)) persists to the time (t') when the outer accretion radius becomes equal to the mean-free path of the SIDM (Ostriker 2000):

$$r_A = \frac{GM_{\rm BH}(t')}{C_s^2} = \lambda = \frac{m_{dm}}{\rho(t')\sigma}, \tag{4}$$

where $m_{\rm dm}$ and σ represent the mass and cross section of the SIDM, respectively, and $\rho(t')$ is the density of the spherical dark matter cloud at time t'. For reasonable values of collisional cross section and particle mass, the cores would naturally grow with black holes of mass (10^8–10^9) $M_\odot$.

Taking $M_{\rm BH}(t') = \frac{4}{3}\pi r_A^3 \rho(t')$ and using Relation (4), we get

$$M_{\rm BH}(t') = \frac{3C_s^4}{4\pi G^2}\frac{\sigma}{m_{dm}}. \tag{5}$$

We can calculate core mass of the black hole at t' considering some appropriate values of C_s, σ, and $m_{\rm dm}$. It has been previously reported that $\frac{\sigma}{m_{dm}} \sim 0.1\,{\rm cm^2\,g^{-1}}$ is eligible for reproducing the core densities of clusters of galaxies, low surface brightness spirals, and dwarf galaxies (Rocha et al. 2013). Whereas observed mass profiles of galaxies demand $\frac{\sigma}{m_{dm}} \sim (0.5\text{–}5)\,{\rm cm^2\,g^{-1}}$ (Tulin & Yu 2017), survival of galaxy clusters requires that $\frac{\sigma}{m_{dm}}$ be less than $1\,{\rm cm^2\,g^{-1}}$ (Markevitch et al. 2004). Therefore, the range of $\frac{\sigma}{m_{dm}}$ to estimate $M_{\rm BH}$ (t') is taken as $0.1\text{–}5\,{\rm cm^2\,g^{-1}}$. The sound speed varies with the temperature of the primordial collapsing cloud as $C_s = 10\sqrt{\frac{T(K)}{10^4\,K}}\ {\rm km\,s^{-1}}$ (Volonteri & Rees 2005). Early phases of supercritical quasi-spherical accretion onto black holes in metal-free halos requires virial temperature $T_{\rm vir} > 10^4$ K (Volonteri & Rees 2005). Considering a range of temperature of the cloud (10^4–10^7) K (Volonteri & Rees 2005), the sound speed is obtained in the range (10–100) ${\rm km\,s^{-1}}$. We take target black holes of mass 10^8 $M_\odot$. The dark matter cross section per unit mass and sound speed are capped at the top accordingly. The upper limit of sound speed is taken $100\,{\rm km\,s^{-1}}$.

The core mass obtained by using Equation (5) is displayed in Table 2. It is evident from Table 2 that for low sound speed, the grown-up (core) masses rise up to (10^5–10^6) $M_\odot$. Black holes of mass (10^5–10^6) $M_\odot$ are of particular interest as the existence of IMBHs of similar masses in dwarf galaxies has been reported (Marel & Bosch 1998; Valluri et al. 2005; Seth et al. 2010; Reines et al. 2013; Mezcua et al. 2018). After the saturation of growth expressed by Equation (4), black holes of this mass do not undergo growth and remain as IMBHs as

Table 2
Core Mass Formed for Different Values of Sound Speed and Specific SIDM Cross Section

C_s (km s^{-1})	$\sigma/m_{\rm dm}$ (cm^2 g^{-1})	$M(t')$ ($M_\odot$)
s 10	0.1	2.68×10^3
	0.5	1.37×10^4
	1	2.68×10^4
	2.5	6.7×10^4
	4	1.07×10^5
	5	1.34×10^5
30	0.1	2.68×10^5
	0.5	1.37×10^6
	1	2.68×10^6
	2.5	6.71×10^6
	4	1.07×10^7
	5	1.34×10^7
100	0.1	2.68×10^7
	0.5	1.37×10^8
	1	2.68×10^8
	2.5	6.71×10^8

found in dwarfs. These black hole masses can also form by the direct-collapse process (Latif et al. 2013). Thus, these two mechanisms may be equally strong theses for formation of massive black holes of the IMBHs. Studies have shown that seed masses with $M > 10^5\ M_\odot$ are also important for the formation of SMBHs. For sound speed of $C_s = 100\ \mathrm{km\ s^{-1}}$ and $\frac{\sigma}{m_{dm}} = 2.5\ \mathrm{cm^2\ g^{-1}}$, we arrive at a saturated black hole mass of $10^8\ M_\odot$. Therefore, sound speeds higher than $100\ \mathrm{km\ s^{-1}}$ are not considered here.

In the present work, we reinvestigate the possibility of the formation of massive black holes (10^3–10^8) $M_\odot$ at high redshift through Bondi accretion of dark matter onto a 20 $M_\odot$ seed black hole. The density profiles of dark matter are chosen as the NFW universal profile, SIS profile, other power-law profiles, and modified isothermal core profiles.

3. Growth of (10^3–10^8) $M_\odot$ Black Holes from a 20 $M_\odot$ Seed with Different Dark Matter Density Profiles inside an SMFP Core

3.1. Mass and Nature of the SMFP Core

We divide the entire SIDM system into three regions: $\lambda > H$ (LMFP regime) in the nearly static extended halo, $\lambda < H$ (SMFP regime) in the fluid-like inner core, and $\lambda = H$ (the transition region).

The mean-free path of the SIDM particles is given by $\lambda = \frac{1}{\rho_0\left(\frac{\sigma}{m_{dm}}\right)}$, and the gravitational scale height is $H = \frac{v}{\sqrt{4\pi G\rho_0}}$, where ρ_0 is the central density of the SIDM halo. The values of central density and velocity dispersion are taken as $\rho_0 = 0.02\ M_\odot\ \mathrm{pc^{-3}}$ and $v = 100$ and $1000\ \mathrm{km\ s^{-1}}$ (Firmani et al. 2001; Balberg & Shapiro 2002). The mean-free path for a range of cross section is displayed in Table 3. For the above values of v and ρ_0, H is found to be 3–30 kpc.

Between the LMFP and SMFP regions, there exists a transition region which occurs at

$$\lambda = H \tag{6}$$

Table 3
Mean-free Path of SIDM Particles (λ) for $\sigma/m_{\rm dm} = (0.1\text{–}5)\ \mathrm{cm^2\ g^{-1}}$

$\sigma/m_{\rm dm}$ (cm^2 g^{-1})	λ (kpc)
0.1	2314
0.5	460
1	230
2.5	92
4	58
5	46

$$\frac{1}{\rho_o\left(\frac{\sigma}{m_{dm}}\right)} = \frac{v}{\sqrt{4\pi G\rho_o}} \tag{7}$$

$$\rho_o = \frac{4\pi G}{v^2\left(\frac{\sigma}{m_{dm}}\right)^2} = \frac{3M_{R_t}}{4\pi R_t^3} \tag{8}$$

$$R_t = \left(\frac{3M_{R_t}v^2\left(\frac{\sigma}{m_{dm}}\right)^2}{16G\pi^2}\right)^{1/3.} \tag{9}$$

Here R_t and M_{R_t} are the size of the transition region and mass of the SMFP core. In this section, the SMFP core masses, transition radii, and respective densities are calculated by taking different dark matter density profiles into account.

3.1.1. NFW Profile and the SMFP Core

In SIDM cosmology, dark matter is assumed to assemble into a self-gravitating spherical halo whose primordial mass distribution matches with that of a collisionless CDM. Cosmological simulations have shown that dark matter core size at $z \simeq 5$ is only a tiny fraction of the size at $z = 0$ (Vogelsberger et al. 2014). Reasonably, at high redshift, the average number of collisions among dark matter particles is found to be less than or equal to 1 per Hubble time. Therefore, the halo profile can be reasonably approximated by the universal profile of CDM, which is given by a two-parameter formula known as the NFW profile (Navarro et al. 1996, 1997).

A generalized NFW profile is expressed as

$$\rho(r) = \frac{\rho_c}{\left(\frac{r}{r_c}\right)^{\alpha}\left(1+\frac{r}{r_c}\right)^{3-\alpha}}, \tag{10}$$

where ρ_c and r_c are scale density and scale radius, respectively. The slope of the profile is defined as $\beta = -\frac{dln\rho(r)}{dlnr}$. For $r \gg r_c$ the slope is $\beta = 3$. For $r \ll r_c$ the slope is $\beta = \alpha$. For the original NFW profile, $\alpha = 1$, and hence, the inner slope is 1, and the profile is singular as $\rho(r) \propto r^{-1}$. Here we discuss the slope of the NFW profile and the scale parameters, ρ_c and r_c.

For $\beta = 1$, the density profile is expressed in terms of critical density and a characteristic overdensity as

$$\rho(r) = \rho_{\rm crit}\frac{\delta_o}{\left(\frac{r}{r_c}\right)\left(1+\frac{r}{r_c}\right)^2}, \tag{11}$$

where the characteristic overdensity is expressed as $\delta_o = \frac{\rho_c}{\rho_{\rm crit}}$, where ρ_c is the scale density and $\rho_{\rm crit} = 277.3\ h^2\ M_\odot\ \mathrm{kpc^{-3}}$ is the background cosmological (critical) density. The halo concentration is defined as $C = \frac{R_{200}}{r_c}$, where R_{200} is the size of the halo when its density is 200 times the background

density and is expressed as $R_{200} = \left(\frac{M_{200}}{\frac{4}{3}\pi\ 200\rho_{\rm crit}}\right)^{1/3}$. Here M_{200} is the mass contained within the halo of radius R_{200}.

From the mass profile

$$M(r) = \int_0^r \rho(r)\ 4\pi r^2\ dr, \tag{12}$$

calculation of M_{200} gives the following relation between δ_o and C:

$$\delta_o = \frac{200C^3}{3}\frac{1}{\ln(1+C) - \left(\frac{C}{1+C}\right)}. \tag{13}$$

Mo et al. (1998) have given the ansatz $5 < C < 30$, whereas galaxy rotation curve studies have excluded very low values of C (Jimenez et al. 2003).

The halo mass (M_{200}) is governed by the halo concentration (C) evaluated at a particular cosmological redshift. The halo mass at a given epoch z is expressed as

$$M_{200} = \frac{4\pi}{3}(200\rho_{\rm crit}(z))R_{200}^3. \tag{14}$$

Here, R_{200} ($= r_{\rm c}C$) is the virial radius, which depends on the scale radius ($r_{\rm c}$) and the halo concentration (C).

$$M_{200} = \frac{4\pi}{3}(200\rho_{\rm crit}(z))r_c^3C^3, \tag{15}$$

where $\rho_{\rm crit}$ is the critical density evaluated at epoch z and is expressed in standard ΛCDM cosmology as

$$\rho_{\rm crit} = \frac{3H(z)^2}{8\pi G} = \frac{3}{8\pi G}H_0^2[\Omega_{m(0)}(1+z)^3 + \Omega_{\Lambda(0)}]. \tag{16}$$

We consider two epochs, $z = 20$ and 30, which correspond to the epochs of initiation of large-scale structure formation. The cosmological parameters are $H_0 \simeq 75\ {\rm km\ s^{-1}\ Mpc^{-1}}$, $\Omega_{\rm m(0)} = 0.3$, and $\Omega_{\Lambda(0)} = 0.7$. The critical densities (from Equation (16)) at $z = 20$ and 30 are found as $4.3 \times 10^5\ M_\odot\ {\rm kpc^{-3}}$ and $1.39 \times 10^6\ M_\odot\ {\rm kpc^{-3}}$, respectively.

We consider galactic-size halos with mass $M_{200} = 10^{12}\ M_\odot$ and massive halos $M_{200} = (10^{13}, 10^{14})\ M_\odot$. This is the range of halo mass required for forming SMBHs with masses greater than or equal to $10^6\ M_\odot$ (see Balberg & Shapiro 2002). The halo concentration C (from Equation (15)), overdensity δ_0 (Equation (13)), and scale density ρ_c ($= \rho_{\rm crit}\delta_0$) are calculated for each halo mass at redshifts $z = 20$ and 30, taking scale radius $r_{\rm c} = 2$ kpc and are shown in Table 5. This value of r_c for the NFW profile has been indicated by observations of optical rotation curves of galaxies (Jimenez et al. 2003). The estimated parameters are displayed in Table 4. The self-consistently derived halo concentrations at redshift $z = 20$ and 30 within chosen values of M_{200} are obtained in the range (4.754–32.58), which is consistent with theoretical ansatz $5 < C < 30$ given by Mo et al. (1998).

The density profile of a core becomes a power law arising from an approximation of the universal NFW profile (see Equation (10)) and is given by

$$\rho(r) = \rho_{\rm crit}\delta_0\left(\frac{r}{r_c}\right)^{-1}. \tag{17}$$

The above profile is for the inner region, where $r \ll r_{\rm c}$ and $\alpha = 1$.

Table 4
Halo Concentration (C), Characteristic Overdensity (δ_0), and Scale Density (ρ_c) for Each Halo Mass (M_{200}) at Two Primordial Epochs ($z = 20,30$)

M_{200} ($M_\odot$)	Z	C	δ_0	ρ_c ($M_\odot\ {\rm pc^{-3}}$)
10^{12}	20	7.018	19100.9	8.246
	30	4.754	7754.63	10.77
10^{13}	20	15.12	125098.4	54
	30	10.24	47454.6	65.89
10^{14}	20	32.58	906346.6	391
	30	22.07	328461.9	456

Therefore, the SMFP core mass (mass enclosed in radius R_t) is obtained from Equation (12) as

$$M_{R_t} = 2\pi\rho_{\rm crit}\delta_o r_c R_t^2. \tag{18}$$

Using Equation (9) in (18), we get

$$M_{R_t} = (2\pi\rho_{\rm crit}\delta_o r_c)^3\left(\frac{3v^2\left(\frac{\sigma}{m_{dm}}\right)^2}{16G\pi^2}\right)^2. \tag{19}$$

The core masses are calculated for the entire range of $\sigma/m_{\rm dm} = (0.1\text{–}5)\ {\rm cm^2\ g^{-1}}$, scale radius $r_{\rm c} = 2$ kpc, and two values of velocity dispersion $v = 100$ and $1000\ {\rm km\ s^{-1}}$. The SMFP core masses must not exceed the halo masses ($10^{12}\ M_\odot$, $10^{13}\ M_\odot$, and $10^{14}\ M_\odot$). The upper limit is precisely around 10^{-2} times the halo mass (Balberg & Shapiro 2002). As our target black holes have the mass window (10^3–10^8) $M_\odot$, we have to have SMFP cores of at least $10^4\ M_\odot$ and upwards. This is because once the accretion exceeds the SMFP core radius, the system enters into the LMFP region. With these two considerations, we estimate the SMFP core masses as follows. In case of $v = 100\ {\rm km\ s^{-1}}$ for both the halo concentrations ($C = 7.018$ and 4.754) of $10^{12}\ M_\odot$, the SMFP core mass falls within (10^5–10^9) $M_\odot$, while the cross section runs from $0.1\ {\rm cm^2\ g^{-1}}$ up to $1\ {\rm cm^2\ g^{-1}}$. For halo concentration ($C = 15.12$ and 10.24) of $10^{13}\ M_\odot$, the SMFP core mass falls within (10^8–10^{11}) $M_\odot$ as the cross section runs from $0.1\ {\rm cm^2\ g^{-1}}$ to $0.5\ {\rm cm^2\ g^{-1}}$. For halo concentration ($C = 32.58$ and 22.07) of $10^{14}\ M_\odot$ the SMFP core mass realized is $10^{10}\ M_\odot$ for cross section $0.1\ {\rm cm^2\ g^{-1}}$. In case of $v = 1000\ {\rm km\ s^{-1}}$ for both the values of halo concentration ($C = 7.018$ and 4.754) of $10^{12}\ M_\odot$, the SMFP core mass is $10^9\ M_\odot$ for cross section $0.1\ {\rm cm^2\ g^{-1}}$. For the other two massive halos, the SMFP core masses are found to be exceedingly large compared to the limit (10^{-2} times the halo mass) for all values of the cross section. Therefore, for the NFW profile, the SIDM cross section is narrowed down to $(0.1\text{–}1)\ {\rm cm^2\ g^{-1}}$ to realize realistic SMFP core masses.

For velocity $v = 100\ {\rm km\ s^{-1}}$, the transition radius R_t (Equation (9)) is obtained in the range (1.247–124.7) pc for the SMFP core masses $M_{R_t} = (10^5\text{–}10^9)\ M_\odot$ ($C = 7.018$, 4.754 for $M_{200} = 10^{12}\ M_\odot$), (12.47–364.69) pc for the SMFP core masses $M_{R_t} = (10^8\text{–}10^{11})\ M_\odot$ ($C = 15.12$, 10.24 for $M_{200} = 10^{13}\ M_\odot$), and 57.89 pc for the SMFP core mass $M_{R_t} = 10^{10}\ M_\odot$ ($C = 32.58$, 22.07 for $M_{200} = 10^{14}\ M_\odot$). Again, for $v = 1000\ {\rm km\ s^{-1}}$, the only realized transition radius is obtained

as 124 pc for the core mass $M_{R_t} = 10^9\ M_\odot$ ($C = 7.018$, 4.754 for $M_{200} = 10^{12}\ M_\odot$).

3.1.2. Power-law Profiles and the SMFP Core

In addition to the NFW profile, we also consider the spike profiles of the SIDM, which is being accreted by the seed black hole. The widely studied SIS was used earlier to estimate the mass of black holes formed by accretion of collisional dark matter (Ostriker 2000). The profile is given by

$$\rho_s = \frac{C_s^2}{2\pi G r^2}, \tag{20}$$

where ρ_s and C_s are the density and sound speed of the dark matter fluid.

Using the above profile in Equation (12), we get the mass of the SMFP core as

$$M_{R_t} = \frac{2C_s^2}{G} R_t. \tag{21}$$

Using R_t from Equation (9) in Equation (21), we get

$$M_{R_t} = \left(\frac{2C_s^2}{G}\right)^{3/2} \left(\frac{3v^2\left(\frac{\sigma}{m_{dm}}\right)^2}{16G\pi^2}\right)^{1/2}. \tag{22}$$

The SMFP core masses and transition radii for velocity dispersion of $v = 100\ \mathrm{km\,s^{-1}}$ are in the ranges $M_{\mathrm{Rt}} = (10^4$–$10^9)\ M_\odot$ and $R_t = (0.58$–$364.69)$ pc. For $v = 1000\ \mathrm{km\,s^{-1}}$ the core masses and transition radii are found to be $(10^5$–$10^{10})\ M_\odot$ and (5.79–3646.9) pc, respectively. The sound speed considered here is $C_s = (10$–$100)\ \mathrm{km\,s^{-1}}$.

We consider other spike profiles guided by the prescription given by Balberg et al. (2002). These authors found that the stable LMFP region acquires a density profile $\rho(r) \propto r^{-\gamma}$ with $\gamma = 2.19$. The profile was reported to be consistent with the N-body simulation of SIDM evolution. Power-law cuspy profiles, different from SIS, have also been studied near the Galactic center black hole to estimate their role in testing gravitational theories (Lalremruati & Kalita 2022). Chan et al. (2022) studied constraints on power-law dark matter profiles through the pericenter shift of the star S2 encircling the Galactic center black hole. These profiles are expressed by the scale quantities ρ', r' as

$$\rho(r) = \rho'\left(\frac{r'}{r}\right)^{\gamma}. \tag{23}$$

The scale density and scale radius have been found empirically through the observed pericenter shift of S2 (Chan et al. 2022). They are $2.24 \times 10^{-14}\ \mathrm{g\,m^{-3}}$ and 0.012 pc, respectively. Although the cusp index (γ) can run from 0.5 to 2.5 (Fields et al. 2014), our preference is $2.19 \leqslant \gamma \leqslant 2.5$. Using Equations (23) and (9) on Equation (12), the core masses for different values of γ are shown below.

For $\gamma = 2.19$,

$$M_{R_t} = \left(\frac{(4\pi)^{0.46}\rho' r'^{2.19}}{0.81}\left(\frac{3v^2\left(\frac{\sigma}{m_{dm}}\right)^2}{G}\right)^{0.27}\right)^{1/0.73}. \tag{24}$$

For $v = 100\ \mathrm{km\,s^{-1}}$, the SMFP core masses and radii are in the range $(10^5$–$10^7)\ M_\odot$ and (2.29–31.08) pc, respectively. These ranges are $(10^6$–$10^7)\ M_\odot$ and (18.75–254.54) pc, respectively, for $v = 1000\ \mathrm{km\,s^{-1}}$.

For $\gamma = 2.3$,

$$M_{R_t} = \left(\frac{(4\pi)^{0.54}\rho' r'^{2.3}}{0.7}\left(\frac{3v^2\left(\frac{\sigma}{m_{dm}}\right)^2}{G}\right)^{0.23}\right)^{1/0.77}. \tag{25}$$

The SMFP core masses for $\gamma = 2.3$ and $v = 100\ \mathrm{km\,s^{-1}}$ and $1000\ \mathrm{km\,s^{-1}}$ are in the range $(10^5$–$10^6)\ M_\odot$. The transition radii for $v = 100$ and $1000\ \mathrm{km\,s^{-1}}$ are found to be in the range (1.57–21.37) pc and (11.56–156.87) pc, respectively.

For $\gamma = 2.4$,

$$M_{R_t} = \left(\frac{(4\pi)^{0.6}\rho' r'^{2.4}}{0.6}\left(\frac{3v^2\left(\frac{\sigma}{m_{dm}}\right)^2}{G}\right)^{0.2}\right)^{1/0.8}. \tag{26}$$

For $\gamma = 2.4$, the SMFP core masses for both values of v are found to be in the range $(10^5$–$10^6)\ M_\odot$. The transition radii for $v = 100$ and $1000\ \mathrm{km\,s^{-1}}$ are found to be in the range (1.64–22.24) pc and (11.17–151.55) pc, respectively.

For $\gamma = 2.5$,

$$M_{R_t} = \left(\frac{(4\pi)^{0.68}\rho' r'^{2.5}}{0.5}\left(\frac{3v^2\left(\frac{\sigma}{m_{dm}}\right)^2}{G}\right)^{0.16}\right)^{1/0.84}. \tag{27}$$

For $v = 100\ \mathrm{km\,s^{-1}}$, the core masses and transition radii are found to be in the range $(10^4$–$10^5)\ M_\odot$ and (1.29–13.98) pc, respectively. For $v = 1000\ \mathrm{km\,s^{-1}}$, the core masses are found to be of the order of $10^5\ M_\odot$ and transition radii in the range (6.40–86.92) pc.

3.1.3. Modified-core Isothermal Profiles and the SMFP Core

A flat core, rather than the steeper profile seen in CDM simulations, is a better representation of the dark matter profiles of low-surface-brightness (LSB) galaxies and some high-surface-brightness galaxies (de Blok et al. 2001; Salucci 2001). Besides the cuspy profiles ($2.19 \leqslant \gamma \leqslant 2.5$), the density profiles of the core of an SIDM halo are considered to be modified-core isothermal profiles, which behave similarly to the isothermal spherical profile with a constant density at the inner core.

A modified isothermal profile with constant density at the inner core is given by Begeman et al. (1991):

$$\rho(r) = \frac{\rho_0 r_0^2}{r^2 + r_0^2}, \tag{28}$$

where r_o is the core radius and ρ_0 is the central dark matter density.

Using the above density profile in Equation (12), the core mass is obtained as

$$M_{R_t} = \frac{9v^2 r_0^2}{G}\left\{\frac{R_t}{r_0} - \tan^{-1}\left(\frac{R_t}{r_0}\right)\right\}. \tag{29}$$

Using the transition radii from Equation (9) in Equation (29), the SMFP core mass is given by

$$M_{R_t} = \frac{9v^2 r_0}{G}\left\{\frac{\left(\frac{3M_{R_t}v^2\left(\frac{\sigma}{m_{dm}}\right)}{16G\pi^2}\right)^{1/3}}{r_0} - \tan^{-1}\left(\frac{\left(\frac{3M_{R_t}v^2\left(\frac{\sigma}{m_{dm}}\right)}{16G\pi^2}\right)^{1/3}}{r_0}\right)\right\}. \quad (30)$$

The values of core radius r_0 and central density ρ_0 are taken as 0.012 pc and $3.3 \times 10^8\ M_\odot\ \mathrm{pc}^{-3}$, respectively (Chan et al. 2022). The numerical solution of Equation (30) gives the SMFP core mass and transition radius for $\sigma/m_{\rm dm} = (0.5\text{–}5)\ \mathrm{cm}^2\ \mathrm{g}^{-1}$ and $v = 100\ \mathrm{km\ s}^{-1}$ as $(10^9\text{–}10^{10})\ M_\odot$ and (100.4–1004.5) pc, respectively. Similarly for $v = 1000\ \mathrm{km\ s}^{-1}$, they are in the ranges $(10^{13}\text{–}10^{14})\ M_\odot$ and (10.045–100.45) kpc, respectively. For $v = 1000\ \mathrm{km\ s}^{-1}$, the core masses are neglected as they are obtained in the range of supergalactic scale.

Another modified-core density profile is given by Brownstein (2009) as

$$\rho(r) = \frac{\rho_0 r_0^3}{r^3 + r_0^3}. \quad (31)$$

Here ρ_0 is the core density, and r_0 is the core radius. Inserting the above profile in Equation (12), the SMFP core mass is obtained as

$$M_{R_t} = [-\log(r_0^3) + \log(r_0^3 + R_t^3)]. \quad (32)$$

The transition radii between the SMFP and LMFP regions, obtained from Equation (9), is used in Equation (32) to evaluate the core mass given as

$$M_{R_t} = \frac{4\pi\rho_0 r_0^3}{3}\left[-\log(r_0^3) + \log\left(r_0^3 + \frac{3M_{R_t}v^2\left(\frac{\sigma}{m_{dm}}\right)}{16G\pi^2}\right)\right]. \quad (33)$$

Taking velocity dispersion $v = 100\ \mathrm{km\ s}^{-1}$ and $1000\ \mathrm{km\ s}^{-1}$ and the above values of r_0 and ρ_0, Equation (33) is solved numerically. The core masses $M_{\rm Rt}$ for $v = 100$ and 1000 $\mathrm{km\ s}^{-1}$ are found to be of the order of $10^5\ M_\odot$ for the entire range of SIDM cross section/mass, $\sigma/m_{\rm dm} = (0.5\text{–}5)\ \mathrm{cm}^2\ \mathrm{g}^{-1}$. The transition radius is found to be in the range (4.55–21.57) pc for $v = 100\ \mathrm{km\ s}^{-1}$ and (21.57–101.88) pc for $v = 1000\ \mathrm{km\ s}^{-1}$.

3.1.4. Fluidty of the SMFP Core

Now we consider a seed black hole of mass $20\ M_\odot$ inside the SMFP core. Such a seed was considered in the original idea of Ostriker (Ostriker 2000) for black hole growth. This is also compatible with the upper bound on the collapsing region inside the SMFP core that finally becomes a black hole (Balberg & Shapiro 2002). Accretion onto this seed is considered for generating the massive black holes.

The accretion radius $r_{\rm A}$ $(= \frac{GM_{\rm BH}}{C_s^2})$ for a $20\ M_\odot$ seed within the range of sound speed (10–100) $\mathrm{km\ s}^{-1}$ is found to be in the range $(10^{-4}\text{–}10^{-5})$ pc, which is much smaller than the transition radius $R_{\rm t}$. Therefore, in the process of collapse, the fluid-like core forms earlier than the termination of accretion.

Any collisional or collisionless gas in virial equilibrium prone to radial instability collapses within the dynamical timescale. As the density of the collapsing system increases, the rate of interaction among the SIDM particles increases. As a result, heat conduction as well as mass loss is halted. Secular instability is terminated, and we have a finite mass black hole (Balberg et al. 2002). Thus, a very large cross section would produce overly massive black holes (see Equation (5)). The values of λ for different $\sigma/m_{\rm dm}$ are displayed in Table 3. It is evident that because $\lambda > H$ during the entire range of $\sigma/m_{\rm dm}$ ($(0.1\text{–}5)\ \mathrm{cm}^2\ \mathrm{g}^{-1}$), the system is still weakly collisional. Therefore, the range $\sigma/m_{\rm dm} = (0.1\text{–}5)\ \mathrm{cm}^2\ \mathrm{g}^{-1}$ is realized not to overproduce a very massive central black hole near the present Universe ($z = 0$).

Table 5
Minimum Halo Density (ρ^*) for $\sigma/m_{\rm dm} = (0.1\text{–}5)\ \mathrm{cm}^2\ \mathrm{g}^{-1}$

$\sigma/m_{\rm dm}$ ($\mathrm{cm}^2\ \mathrm{g}^{-1}$)	ρ^* ($\mathrm{g\ cm}^{-3}$)	
	$V = 100\ \mathrm{km\ s}^{-1}$	$V = 1000\ \mathrm{km\ s}^{-1}$
0.1	8.38×10^{-19}	8.38×10^{-21}
0.5	3.35×10^{-20}	3.35×10^{-22}
1	8.38×10^{-21}	8.38×10^{-23}
2.5	1.34×10^{-21}	1.34×10^{-23}
4	5.24×10^{-22}	5.24×10^{-24}
5	3.35×10^{-22}	3.35×10^{-24}

For a smaller mean-free path, i.e., $\lambda < \mathrm{H}$, the minimum limit on the SIDM halo density is given by

$$\rho > \rho^* = \frac{4\pi G}{\left(v\left(\frac{\sigma}{m_{dm}}\right)\right)^2}. \quad (34)$$

The values of central density and velocity dispersion are $\rho_0 = 0.02\ \ M_\odot\ \ \mathrm{pc}^{-3}$ and $v = 100$ and $1000\ \mathrm{km\ s}^{-1}$. The corresponding minimum SIDM halo densities (ρ^*) are displayed in Table 5.

The black hole density for a $20\ M_\odot$ seed accreting within a radius r_A is $\rho_{\rm BH} = \frac{3M_{\rm BH}}{4\pi r_A^3}$. The black hole densities calculated for different accretion radius, obtained for different values of sound speed C_s are found to be in the range $(10^{-13}\text{–}10^{-10})\ \mathrm{g\ cm}^{-3}$. The SMFP core density $\left(\rho_{\rm SMFP} = \frac{3M_{R_t}}{4\pi R_t^3}\right)$ in the NFW profile for $v = 100\ \mathrm{km\ s}^{-1}$ is found in the range $(10^{-19}\text{–}10^{-21})\ \mathrm{g\ cm}^{-3}$ for $M_{200} = 10^{12}\ M_\odot$, $(10^{-19}\text{–}10^{-20})\ \mathrm{g\ cm}^{-3}$ for $M_{200} = 10^{13}\ M_\odot$ and $10^{-19}\ \mathrm{g\ cm}^{-3}$ for $M_{200} = 10^{14}\ \ M_\odot$. Similarly, for $v = 1000\ \mathrm{km\ s}^{-1}$, the core density is found to be $10^{-21}\ \mathrm{g\ cm}^{-3}$ for $M_{200} = 10^{12}\ M_\odot$. For the SIS profile, the core densities are found to be in the range $(10^{-18}\text{–}10^{-21})\ \mathrm{g\ cm}^{-3}$ for $v = 100\ \mathrm{km\ s}^{-1}$ and $(10^{-20}\text{–}10^{-23})\ \mathrm{g\ cm}^{-3}$ for $v = 1000\ \mathrm{km\ s}^{-1}$. The SMFP core densities for $\gamma = 2.19$ are in the range $(10^{-17}\text{–}10^{-20})\ \mathrm{g\ cm}^{-3}$ and $(10^{-19}\text{–}10^{-22})\ \mathrm{g\ cm}^{-3}$ for $v = 100\ \mathrm{km\ s}^{-1}$ and $1000\ \mathrm{km\ s}^{-1}$, respectively. The core densities are found to be $(10^{-18}\text{–}10^{-20})\ \mathrm{g\ cm}^{-3}$ and $(10^{-20}\text{–}10^{-22})\ \mathrm{g\ cm}^{-3}$ for $v = 100\ \mathrm{km\ s}^{-1}$ and $1000\ \mathrm{km\ s}^{-1}$, respectively, for both values of $\gamma = 2.3$ and $\gamma = 2.4$. And for $\gamma = 2.5$, it is in the range $(10^{-18}\text{–}10^{-21})\ \mathrm{g\ cm}^{-3}$ for $v = 100\ \mathrm{km\ s}^{-1}$ and $(10^{-20}\text{–}10^{-23})\ \mathrm{g\ cm}^{-3}$. The SMFP core densities for both the modified-core isothermal profiles given by Equations (28) and (31) are obtained in the ranges $(10^{-20}\text{–}10^{-22})\ \mathrm{g\ cm}^{-3}$ for $v = 100\ \mathrm{km\ s}^{-1}$ and $(10^{-22}\text{–}10^{-24})\ \mathrm{g\ cm}^{-3}$ for $v = 1000\ \mathrm{km\ s}^{-1}$. We compare the black hole densities ($\rho_{\rm BH}$) and the SMFP core density ($\rho_{\rm SMFP}$) obtained for every value of cross section with the corresponding minimum

halo density (ρ^*) calculated for $v = 100\,\mathrm{km\,s^{-1}}$ and $1000\,\mathrm{km\,s^{-1}}$. It is found that for a 20 $M_\odot$ seed black hole, $\rho_{\rm BH} > \rho^*$ for both values of v. Similarly, the SMFP core density for the power-law NFW profile becomes comparable to the minimum density required for a fluid-like behavior ($\rho_{\rm SMFP} \simeq \rho^*$). Also, the SMFP core densities satisfy the inequality $\rho_{SMFP} > \rho^*$ for SIS, cuspy power law ($2.19 \leqslant \gamma \leqslant 2.5$), and the modified isothermal profiles. Therefore, the SMFP region behaves as a fluid core. The fluid model thus preserves its character for a shorter mean-free path ($\lambda <$ H) regime, i.e., in the inner region of the SIDM halo irrespective of the dark matter density profile.

3.2. Stability of the LMFP Core

Gravothermal collapse of the SIDM halo first leads to an LMFP core that participates in particle evaporation (mass loss) and hence, heat conduction throughout its volume (Balberg et al. 2002). The late time effect is to produce a shrinking core, leading to formation of the SMFP region, a tiny portion of which collapses under relativistic instability to form the massive black hole. It has been found in earlier investigation that only 10^{-8}–10^{-6} of the total halo mass undergoes dynamical instability to form black holes (Balberg & Shapiro 2002). For a galactic-size ($10^{12}\,M_\odot$) halo, this amounts to 10^4–$10^6\,M_\odot$, which is quite small compared to the SMFP core masses (see Section 3.1.1). The extended halo, which is still in the LMFP regime, however, remains stable against collapse. It is shown by invoking the classical Jeans criterion for collapse. A medium of mass M, ambient temperature T, and density ρ is stable against gravitational collapse if the gravitational pressure is less than the thermal pressure:

$$GM^{2/3}\rho^{4/3} < \rho k_B T/m. \tag{35}$$

Here m is the mass of the constituent particles. In this case, it is the dark matter particle mass. In terms of velocity dispersion of the dark matter particles $v^2 \approx k_B T/m$, the above criterion for stability becomes

$$\frac{GM^{2/3}\rho^{1/3}}{v^2} < 1. \tag{36}$$

The mass of the extended core in the LMFP regime is around $10^{-3}M_{\rm tot}$, M_{tot} being the total halo mass. For halos with $M_{\rm tot} = (10^{12}$–$10^{14})M_\odot$, the LMFP core mass lies in the range $M_{\rm LMFP} = (10^9$–$10^{11})M_\odot$. For the core density of $\rho_0 \approx 0.02\ M_\odot\ \mathrm{pc^{-3}}$, $\frac{GM^{\frac{2}{3}}\rho^{\frac{1}{3}}}{v^2} \approx 10^{-3}$ and 10^{-1}, respectively, for velocity dispersion $v = 1000\,\mathrm{km\,s^{-1}}$ and $100\,\mathrm{km\,s^{-1}}$. Therefore, the LMFP region remains stable against gravitational collapse. It is this region that supplies dark matter to the accreting seed black hole inside the SMFP core during the growth of a massive black hole.

3.3. Stability of Seeds in the Dark Matter Halo

The stability of a compact object moving in a gas of other gravitating particles was first studied by Chandrasekhar (1943). The dynamical friction decelerates the subject body. The timescale within which the compact object settles down in the center is known as dynamical friction time and is expressed by Binney & Tremaine (1987)

$$t_{df} = \frac{1.65 r_i^2\,\sigma}{\ln\Lambda\ (GM_{\rm BH})} = \frac{19\ \mathrm{Gyr}}{\ln\Lambda}\left(\frac{r_i}{5\ \mathrm{Kpc}}\right)^2 \frac{\sigma}{200\ \mathrm{km\ s^{-1}}} \frac{10^8\,M_\odot}{M_{\rm BH}}, \tag{37}$$

where $\Lambda = \left(\frac{M}{M_{\rm BH}}\right)\left(\frac{r_i}{R_h}\right)$.

Equation (37) is the independent of the dark matter density profile. Here M and R_h are the mass and radius of the host halo, and r_i is the orbital radius of the compact object (here 20 $M_\odot$) at $t = 0$. Sigma is the velocity dispersion inside the halo, which is taken as (100–1000) $\mathrm{km\,s^{-1}}$. We assume that the seed mass (20 $M_\odot$) forms within the bulge of the primordial galaxy, which can be taken as the one of a few kiloparsecs in size. For convenience, we take it as 5 kpc. By taking the typical halo radius as $R_h = 100$ kpc, the dynamical friction timescale is found to be much larger than the Hubble time. Thus, the seed (20 $M_\odot$) cannot be stabilized even in the presence of dynamical friction, and hence it keeps on moving through scattering by other stars and dense gas clouds. Therefore, we have to consider the velocity of the seeds while it accretes.

Simulations show that if the SIDM component is considered in place of CDM, it produces a "cored" dark matter profile, which further alters the dynamical friction time and produces off-center black holes (Di Cintio et al. 2017). It has been found to carry potential implication for black hole merger and growth (Cruz et al. 2021).

Seeds with masses from few tens of solar masses to $10^7\,M_\odot$ cannot sink to the center of a halo as their dynamical friction timescales are much larger than the Hubble time. One possibility is ejection of the seed. It is reasonable to speculate that ejection becomes less likely as dark matter is self-interacting and the seed moves in a SIDM halo where sufficient interaction can prohibit evaporation (analogous to globular clusters where star ejection is inhibited by binary formation). Therefore, we consider our seed to be moving and accreting dark matter within the halo to grow into massive black holes (10^3–10^8) $M_\odot$. Once the black hole has grown massive enough ($10^8\,M_\odot$), it eventually spirals to the center of the host halo within about 3 Gyr. Black holes more massive than $10^8\,M_\odot$ formed within 10 kpc eventually sink to the center of the SIDM halo. Those black holes that cannot sink to the center ((20–10^7) $M_\odot$) may very well reside in the outskirts of the halo as wandering black holes (Villalba et al. 2020; Ricarte et al. 2021).

4. Timescale of Formation of (10^3–10^8) $M_\odot$ Black Holes from 20 $M_\odot$ Seed with Different Dark Matter Density Profile

For calculating the timescales of growth from a seed mass of 20 $M_\odot$ into massive black holes (10^3–10^8) $M_\odot$, we consider NFW, SIS, other power-law profiles ($2.19 \leqslant \gamma \leqslant 2.5$), and modified-core isothermal profiles of accreted dark matter. The reason we use the NFW dark matter profile is that it is valid for widely different mass scales being independent of dark matter halo mass, primordial density fluctuations, and values of the cosmological parameters. If dark matter halo mass is contributed by 100 GeV weakly interacting massive particles, then it has been recently shown that a dark matter halo with an NFW profile can span a halo mass range (10^{-6}–10^{15}) $M_\odot$ (Wang et al. 2020). Choquette et al. (2019) explained early formation of SMBHs with the help of two-component dark matter (CDM + (subdominant) SIDM) satisfying an initial NFW profile. These authors simulated gravothermal collapse of an initial NFW dark matter halo by using the GADGET N-body

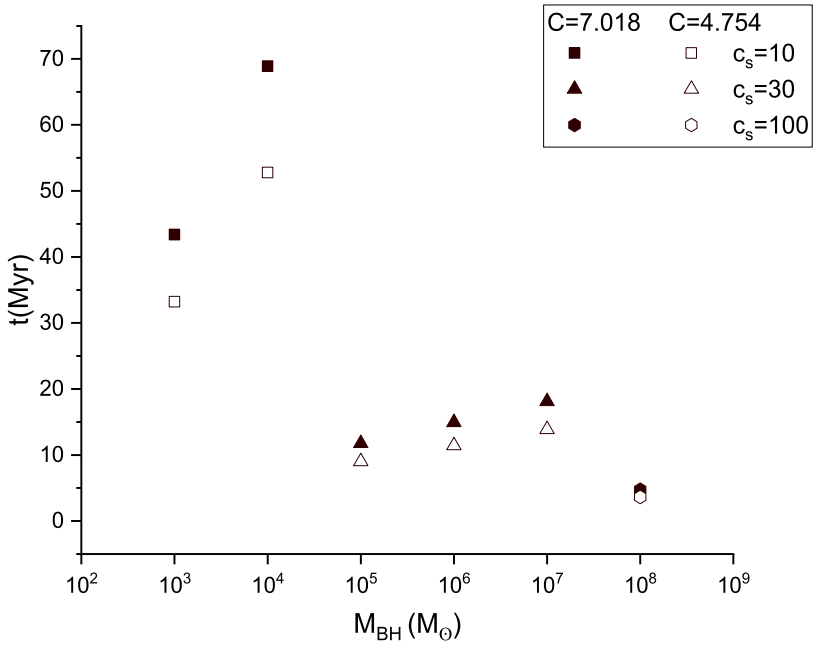

C=7.018 Zi=20	C=4.754 Zi=30
zf	zf
1. 17.17	17.748
2. 15.9	16.679
3. 19.12	19.324
4. 18.91	19.150
5. 18.69	18.981
6. 19.63	19.719

Figure 1. Formation timescale of (10^3–10^8) $M_\odot$ black holes in NFW profile with halo mass $M_{200} = 10^{12}\ M_\odot$ and halo concentration 7.018 and 4.754 corresponding to $z = 20$ and 30, respectively.

simulation code and explained the formation of high-redshift massive black holes by adding a small component of SIDM.

It is generally agreed that the problem of dark matter density profile is yet to be closed. The logarithmic slope β, of the original NFW profile (with $\alpha = 1$), changes from 1 near the center ($r \ll r_c$) to 3 at larger radii ($r \gg r_c$; Mo et al. 1997). This profile is cuspy and usually leads to the core-cusp problem (Moore 1994; Moore et al. 1999; De Blok 2010) when one considers observed diffuse core of LSB galaxies and dwarf galaxies. Less cuspy or core density profiles are modeled as $\beta < 1$. For example, dwarf galaxies show $\beta \approx 0.29$ (Oh et al. 2011), and LSB galaxies show $\beta \approx 0.2$ (de Blok et al. 2001). In a study of collisional dark matter density profile near SMBHs (Guzman & Lora-Clavijo 2011), it has been reported that $\beta < 0.3$. Aligning with these considerations, we estimated the timescale of the formation of (10^3–10^8) $M_\odot$ black holes from a 20 $M_\odot$ seed black hole by taking less cuspy slopes, $\beta = 0.75$, 0.5, and 0.25. All of these slopes produce NFW-type shape ($\beta = 3$) at larger scales. But they are less cuspy (diffuse) toward the center relative to the inner slope of the original NFW profile (also see McMillan 2017 for $\alpha < 1$ representing core-like configuration), thereby resembling collisional dark matter. It has been found that black hole growth is not possible within the Hubble time for these diffuse profiles. Only the original slope $\beta = 1$ gives reasonable timescale of formation of the black holes (see below).

For the slope $\beta = 1$, Equations (11) and (3) imply the following expression for the accretion rate:

$$\dot{M}_{\rm BH} = \frac{4\pi G^2 M_{\rm BH}^2}{(v_s^2 + c_s^2)^{3/2}} \frac{\rho_c}{\frac{GM_{\rm BH}}{c_s^2 r_c}\left(1 + \frac{GM_{\rm BH}}{c_s^2 r_c}\right)^2}. \tag{38}$$

Here, v_s is the velocity of the 20 $M_\odot$ seed black hole.

Integrating the above equation from an initial mass M^* to the black hole mass $M_{\rm BH}(t')$, we get

$$\int_{M^*}^{M_{\rm BH}(t')} \frac{(v_s^2 + c_s^2)^{3/2}}{4\pi G r_c \rho_c c_s^2} \frac{\left(1 + \frac{GM_{\rm BH}}{c_s^2 r_c}\right)^2 dM_{\rm BH}}{M_{\rm BH}} = \int_0^{t'} dt. \tag{39}$$

From Equation (39) we deduce the time required for formation of the massive black hole as

$$t' = \frac{(v_s^2 + c_s^2)^{3/2}}{4\pi G r_c \rho_c c_s^2}\left[\ln\left(\frac{M_{\rm BH}(t')}{M^*}\right) + \frac{G^2}{2C_s^4 r_c^2}(M_{\rm BH}^2(t') - M^{*2}) + \frac{2G}{C_s^2 r_c}(M_{\rm BH}(t') - M^*)\right]. \tag{40}$$

Here, M^* is the initial seed mass that grows to become a grown-up black hole of mass (10^3–10^8) $M_\odot$. This initial seed is considered to be a stellar black hole of mass $\sim$20 $M_\odot$. The reason for the above considered mass of the seed is that various numerical approaches to obtain the black hole mass function over different cosmic times predict the presence of black holes of masses of few tens of solar masses. One such model (Sicilia et al. 2022) shows that the black hole mass function, as a function of the remnant mass, remains constant for $M \sim$ (5–50) $M_\odot$ at redshifts $z \sim$0–10, and most of the black hole mass density is contributed by black holes of mass $M \sim$(20–30) $M_\odot$. We choose the typical velocity of the seed inside the halo as $v_s = 100\ {\rm km\ s^{-1}}$.

The timescale of formation of black hole masses in the range (10^3–10^8) $M_\odot$ is displayed in Figure 1 for halo concentration $C = 7.018$ and $C = 4.754$ ($M_{200} = 10^{12}\ M_\odot$), Figure 2 for halo concentration $C = 15.12$ and $C = 10.24$ ($M_{200} = 10^{13}\ M_\odot$), and Figure 3 for halo concentration $C = 32.58$ and $C = 22.07$ ($M_{200} = 10^{14}\ M_\odot$). It falls in the window (4.77–68.9) Myr for $C = 7.018$, (3.65–52.79) Myr for $C = 4.754$, (0.73–10.5) Myr for $C = 15.12$, (0.59–8.63) Myr for $C = 10.24$, (0.1–1.45) Myr for $C = 32.58$, and (0.86–1.25) Myr for $C = 22.07$. On the other hand, for all other slopes (0.75, 0.5, and 0.25) the timescales are found to be more than or equal to few tens of Gyr. Therefore, we consider only the original slope $\beta = 1$ for presenting our results.

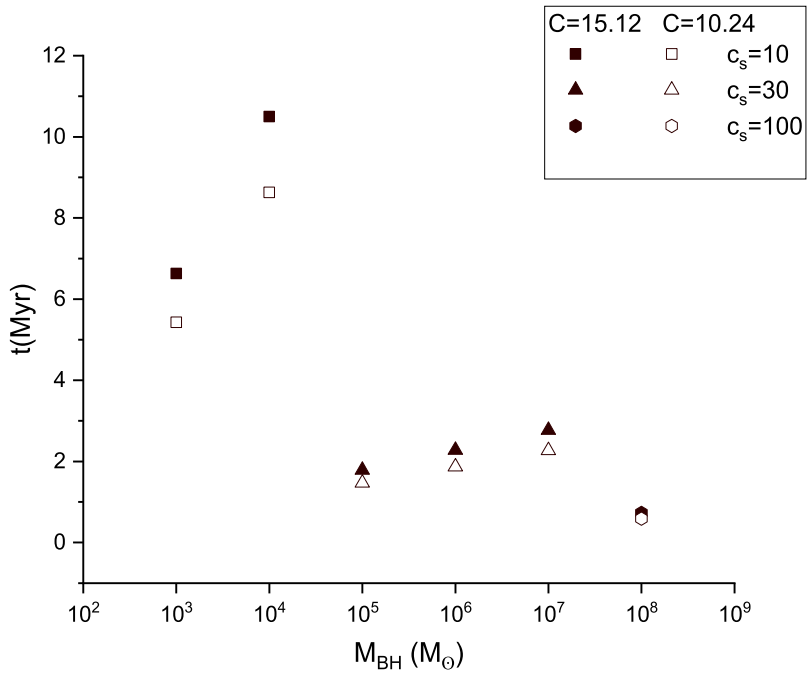

C=15.12 Zi=20	C=10.24 Zi=30
zf	zf
1. 19.49	19.586
2. 19.22	19.352
3. 19.86	19.886
4. 19.82	19.855
5. 19.78	19.824
6. 19.94	19.954

Figure 2. Formation timescale of (10^3–10^8) $M_\odot$ black holes in NFW profile with halo mass $M_{200} = 10^{13}\ M_\odot$ and halo concentration 15.12 and 10.24 corresponding to $z = 20$ and 30, respectively.

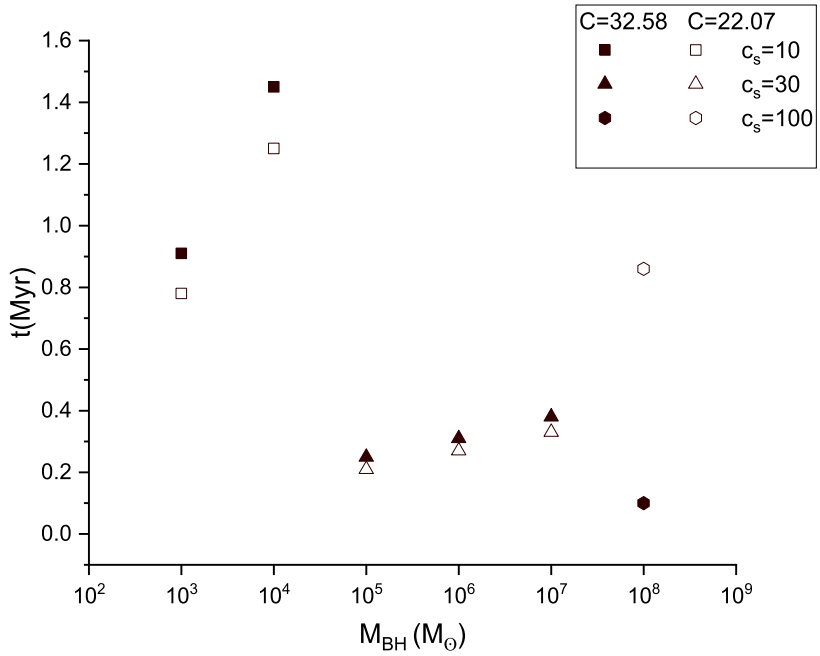

C=32.58 Zi=20	C=22.07 Zi=30
zf	zf
1. 19.93	19.939
2. 19.89	19.903
3. 19.98	19.983
4. 19.976	19.978
5. 19.97	19.974
6. 19.99	19.33

Figure 3. Formation timescale of (10^3–10^8) $M_\odot$ black holes in NFW profile with halo mass $M_{200} = 10^{14}\ M_\odot$ and halo concentration 32.58 and 22.07 corresponding to $z = 20$ and 30, respectively.

For SIS, inserting the density profile given by Equation (20) in Equation (3) and using Equation (4), we get

$$dM_{\rm BH} = \frac{2C_s^6}{(v_s^2 + C_s^2)^{3/2} G}\, dt. \tag{41}$$

Integrating the above, we get the following timescale

$$t = \frac{(v_s^2 + C_s^2)^{3/2} G}{2C_s^6} M_{\rm BH}. \tag{42}$$

The timescales of formation of the black holes (10^3 –10^8) $M_\odot$ are found to be exceptionally short ((0.33–33) Myr) compared to those realized in case of NFW profiles (see Figure 4). It has been observed from Figure 4 that with increasing black hole mass, the timescales for black hole growth increases. and this pattern is prominent for lower value of sound speed.

For power-law profiles with $2.19 < \gamma < 2.5$, plugging Equation (23) in the rate Equation (3), the formation timescales of the (10^3–10^8) $M_\odot$ black holes are calculated. The timescale

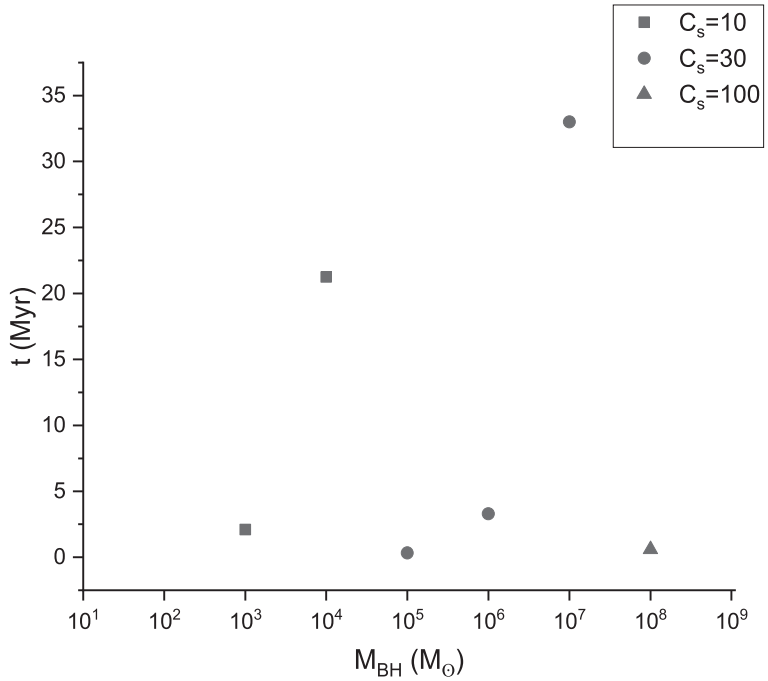

z_i	z_f
1 20	19.84
30	29.57
2 20	18.49
30	26.26
3 20	19.97
30	29.93
4 20	19.74
30	29.33
5 20	17.76
30	24.63
6 20	19.95
30	29.88

Figure 4. Formation timescale of (10^3–10^8) $M_\odot$ black holes in SIS profile of dark matter.

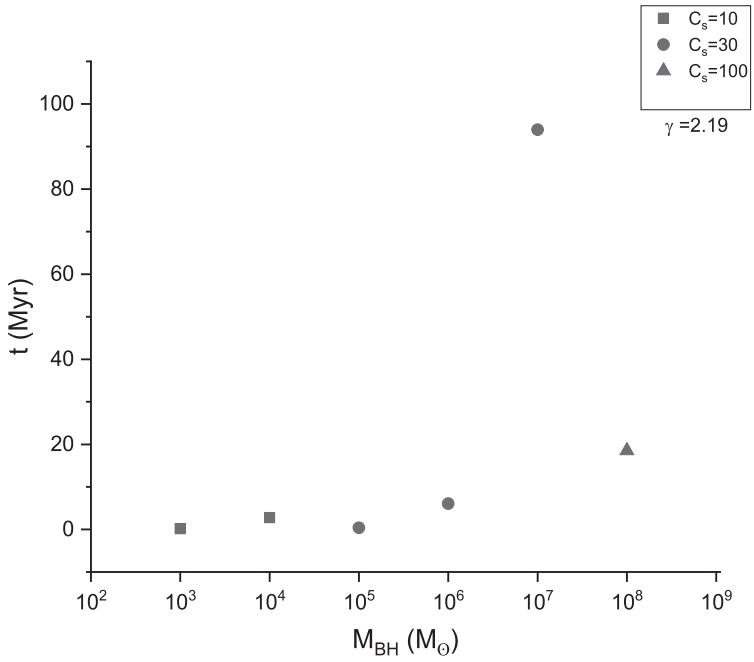

z_i	z_f
1 20	19.98
30	29.96
2 20	19.78
30	24.44
3 20	19.97
30	29.92
4 20	19.54
30	28.80
5 20	14.85
30	18.92
6 20	18.66
30	26.67

Figure 5. Formation timescales of (10^3–10^8) $M_\odot$ black holes in power-law profile with $\gamma = 2.19$.

of formation of the black holes for the cusp indices 2.19, 2.3, 2.4, and 2.5 is shown in Figures 5–8. It has been seen that for low sound speed, the black hole growth timescales increases with the power law index (γ).

The timescales of black hole formation are also calculated for both modified-core isothermal density profiles. The modified isothermal profiles given by Equations (28) and (31) are inserted in the rate Equation (3). For modified-core profile given by Equation (28), the timescales of the formation of black holes are shown in Figure 9. Here also, it is evident from Figure 9 that for a given sound speed, the black hole growth timescales increases with black hole mass. For the modified profile given by Equation (31), the black hole formation timescales are shown in Figure 10. From Figure 10, it is observed that for lower sound speed, the lower mass black holes grow within a timescale smaller than the Hubble time compared to the massive black holes.

The epochs of formation of the black holes are estimated as follows. We consider the standard flat ΛCDM cosmology with model parameters $H_o = 67.4\,\mathrm{km\,s^{-1}\,Mpc^{-1}}$ (Planck Collaboration et al. 2020), $\Omega_m = 0.3$, and $\Omega_\Lambda = 0.7$. The time interval between two redshifts z_i (primordial) and z_f (epoch of formation

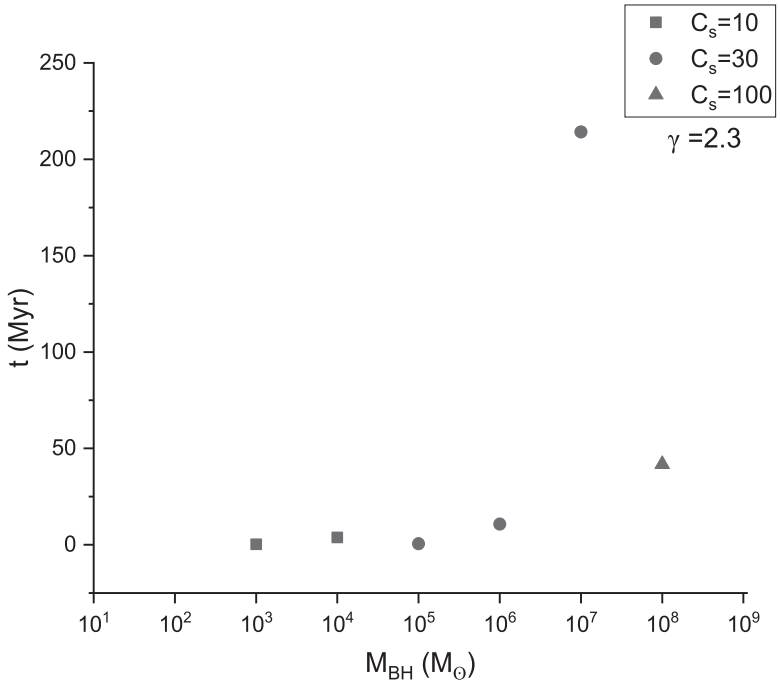

z_i	z_f
1 20	19.98
30	29.96
2 20	19.71
30	29.24
3 20	19.96
30	29.89
4 20	19.20
30	27.96
5 20	11.43
30	13.44
6 20	17.26
30	23.56

Figure 6. Formation timescales of (10^3–10^8) $M_\odot$ black holes in power-law profile with $\gamma = 2.3$.

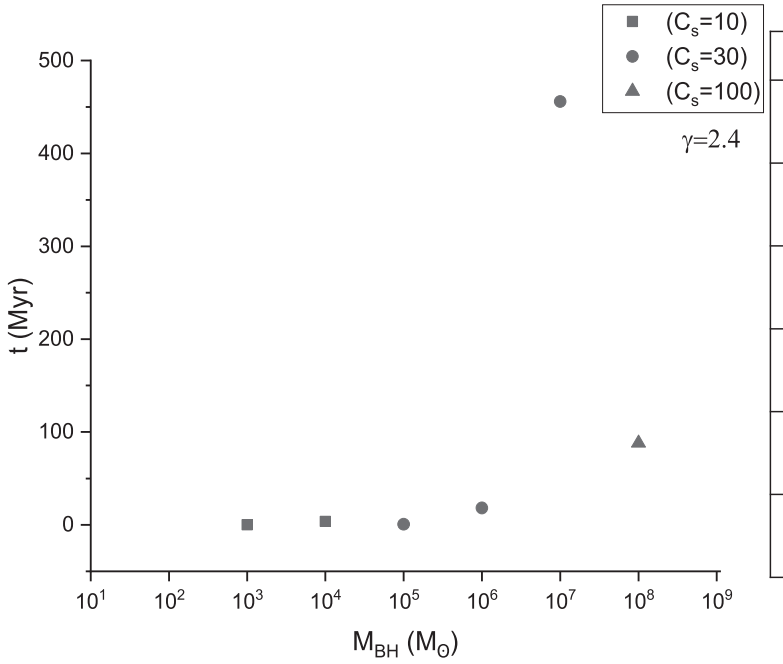

z_i	z_f
1 20	19.98
30	29.96
2 20	19.71
30	29.24
3 20	19.96
30	29.89
4 20	18.69
30	26.73
5 20	8.03
30	8.87
6 20	15.09
30	19.34

Figure 7. Formation timescales of (10^3–10^8) $M_\odot$ black holes in power-law profile with $\gamma = 2.4$.

of the black hole) is given by

$$\Delta t = \frac{1}{H_o}\int_{z_f}^{z_i} \frac{dz}{(1+z)\sqrt{(0.3(1+z)^3+0.7)}}. \quad (43)$$

We consider the primordial epochs $z_i = 20,30$. The reason for considering the primordial epoch z_i to be 20–30 is that in ΛCDM cosmology large structures in the Universe form due to hierarchical merger of smaller building blocks, and the process was initiated at redshift of $z = 20$–30 (Bromm 2013). In addition, the process of the formation of massive black holes and associated quasars is assumed to get initiated well before the epoch of reionization, and it is usually taken as $z_i = 20$–30 (Melia & McClintock 2015). The epoch of formation (z_f) of the (10^3–10^8) $M_\odot$ black holes are displayed in an array adjacent to Figures 1–7. For the NFW profile, it is found that within the range of sound speed $C_s = (10\text{–}100)\,\mathrm{km\,s^{-1}}$, all the values of halo concentration obtained for halo masses (10^{12}–10^{14}) $M_\odot$ at two primordial epochs $z = 20$ and 30 favor the formation of a black hole (10^3–10^8) $M_\odot$ at very high redshifts, well above the highest reported quasar redshift $z = 6$–7 (see Figures 1–3 and the adjacent arrays for redshifts). For SIS, the redshift interval (z_f–z_i) is negligibly small as the black holes form within

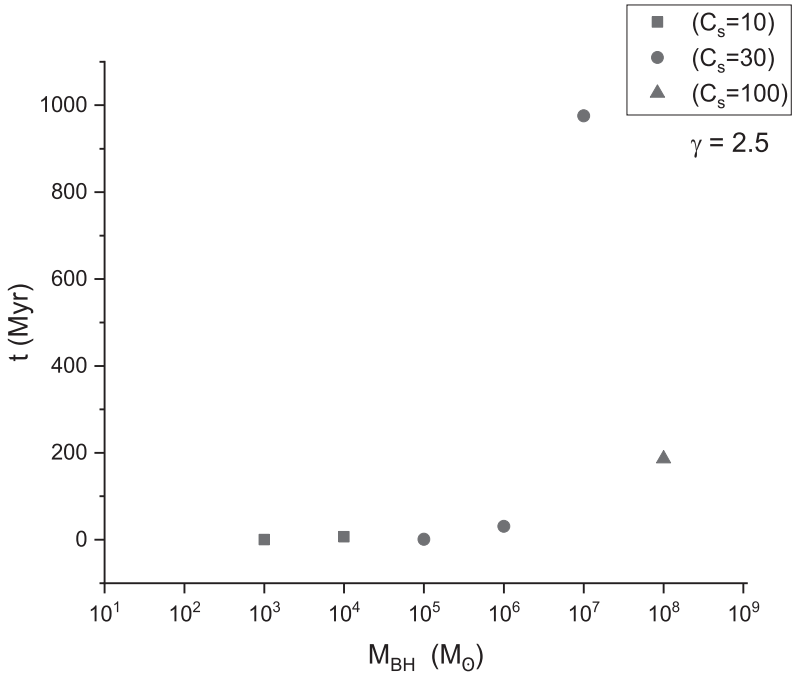

z_i	z_f
1 20	19.98
30	29.95
2 20	19.49
30	29.69
3 20	19.92
30	29.80
4 20	17.89
30	24.91
5 20	5.06
30	5.35
6 20	12.05
30	14.37

Figure 8. Formation timescales of (10^3–10^8) $M_\odot$ black holes in power-law profile with $\gamma = 2.5$.

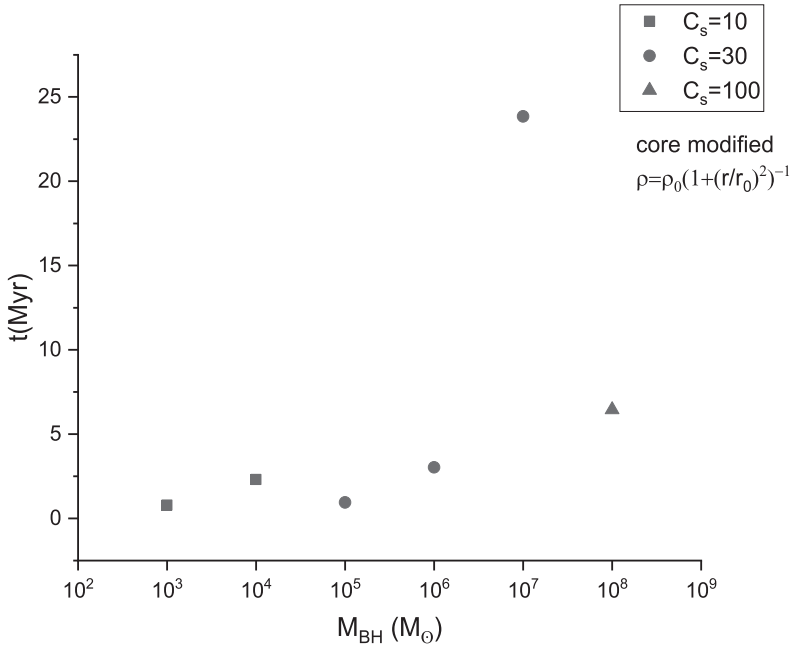

z_i	z_f
1 20	19.94
30	29.96
2 20	19.82
30	29.51
3 20	19.93
30	29.80
4 20	19.77
30	29.39
5 20	18.32
30	25.88
6 20	19.51
30	28.73

Figure 9. Formation timescales of (10^3–10^8) $M_\odot$ black holes in modified-core isothermal profile ($\rho_0(1 + (r/r_0)^2)^{-1}$).

(0.33–33.01) Myr (see Figure 4 and its array). For other power-law profiles, the massive black holes (10^6–10^8) $M_\odot$ form within z_f = (5.05–27.96; see the arrays for Figures 5–8). In the modified-core isothermal density profile given by Equation (28), (10^3–10^8) $M_\odot$ black holes form within a very short span of time (0.79–23.85) Myr (see the array of Figure 9). For the modified-core profile given by Equation (31), (10^3–10^5) $M_\odot$ black holes take (0.93–30.77) Myr to form, whereas 10^6 $M_\odot$ black holes takes 464.08 Myr to form within $z_f = 7.95$ if initiated at $z_i = 20$ (see the array of Figure 10). But the formation timescales for massive black holes 10^7 $M_\odot$ and 10^8 $M_\odot$ are found to be much larger than the Hubble time, and hence, they do not appear in Figure 10.

How rare (massive) should a halo be to host such a growth scenario of massive black holes? A strong relation between the black hole mass and the mass of the host bulge for 49 quasi-stellar objects at $z = 6$ is presented in Shimasaku & Izumi (2019). The median ratio of the black hole to host halo mass for the sample of quasars is reported as 6.3×10^{-4}. The observed sample of quasars satisfies the dark matter halo mass function. Simulations also show that halos as massive as 10^{12} $M_\odot$ can host black holes up to 10^9 (Costa et al. 2014). The threshold

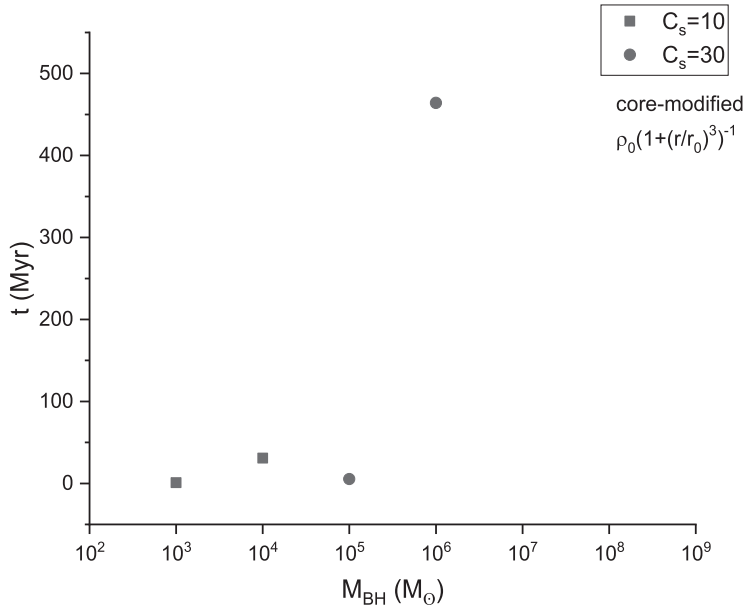

z_i	z_f
1 20	19.93
30	29.81
2 20	17.89
30	24.92
3 20	19.59
30	28.94
4 20	7.95
30	8.77

Figure 10. Formation timescales of (10^3–10^6) $M_\odot$ black holes in modified-core isothermal profile ($\rho_0(1 + (r/r_0)^3)^{-1}$).

masses of quasar hosts are reported as ((2–5) × 10^{12}, (2–5) × 10^{11}, and (1–3) × 10^{11}) $M_\odot$ for median luminosities (10^{46}, 10^{46}, and 10^{45}) erg s^{-1} at redshift $z = (3.2,\ 1.4,$ and $0.53)$ respectively in Cen & Safarzadeh (2015).

5. Results and Discussion

In this work, we have reported the origin of massive black holes with mass range (10^3–10^8) $M_\odot$ through dark matter accretion onto a stellar-mass moving seed black hole. We considered HLB quasi-spherical accretion of SIDM with mass profile taken as the universal NFW profile with inner slope $\beta = 1$, SIS, power-law profiles with cusp index (γ) in the range 2.19–2.5, and two modified-core isothermal profiles. We consider the available bounds on the SIDM-specific cross section $\sigma/m_{\rm dm} = (0.1$–$5)$ cm^2 g^{-1} and the ambient sound speed $C_s = (10$–$100)$ km s^{-1}. Velocity dispersion was taken as $v = 100$ km s^{-1} and 1000 km s^{-1}. The growth of the black holes (10^3–10^8) $M_\odot$ from a 20 $M_\odot$ seed inside an SMFP core has been studied. For the NFW profile, we considered the halo mass range (10^{12}–10^{14}) $M_\odot$ at two primordial redshifts $z = 20$ and 30. The mass of the SMFP cores and the corresponding transition radii are evaluated. In the case of the NFW profile, the halo concentration (C) is calculated for halo masses 10^{12} $M_\odot$, 10^{13} $M_\odot$, and 10^{14} $M_\odot$ and is found to be 7.018, 15.12, and 32.58, respectively, at epoch $z = 20$ and 4.754, 10.24 and 22.07, respectively, at epoch $z = 30$. The SMFP core mass and transition radii for $v = 100$ km s^{-1} are found to be $M_{\rm Rt} = (10^5$–$10^9)$ $M_\odot$ and $R_t = (1.247$–$124.7)$ pc, respectively, for $C = 7.018$,4.754; $M_{\rm Rt} = (10^8$–$10^{11})$ $M_\odot$ and $R_t = (12.47$–$364.69)$ pc, respectively, for $C = 15.12$,10.24; and $M_{\rm Rt} = 10^{10}$ $M_\odot$ and $R_t = 57.89$ pc, respectively, for $C = 32.58$,22.07. The SMFP core mass and transition radii for $v = 1000$ km s^{-1} is found to be $M_{\rm Rt} = 10^9$ $M_\odot$ and $R_t = 124.725$ pc, respectively, for $C = 7.018,\ 4.754$. Realistic SMFP core masses in the NFW profile are realized for a narrow range of SIDM cross section $\sigma/m_{\rm dm} = (0.1$–$1)$ cm^2 g^{-1}. The SMFP core masses and transition radii for the SIS profile are found to be $M_{\rm Rt} = (10^4$–$10^9)$ $M_\odot$ and $R_t = (0.58$–$364.69)$ pc, respectively, for $v = 100$ km s^{-1} and $M_{\rm Rt} = (10^5$–$10^{10})$ $M_\odot$ and $R_t = (5.79$–$3646.9)$ pc, respectively, for $v = 1000$ km s^{-1}. For the two velocity dispersion values, the SMFP core masses and transition radii are found to be in the range $M_{\rm Rt} = (10^4$–$10^7)$ $M_\odot$ and $R_t = (1.29$–$254.54)$ pc, respectively, for the entire range of the cusp index ($2.19 \leqslant \gamma \leqslant 2.5$). As the SMFP core mass decreases with cusp index, the power-law profiles with larger cusp indices prefer formation of low-mass seeds. For the modified-core profile given by Equation (28), the SMFP core masses and transition radii are obtained as $M_{\rm Rt} = (10^9$–$10^{10})$ $M_\odot$ and $R_t = (100.4$–$1004.57)$ pc, respectively, for $v = 100$ km s^{-1} and $M_{\rm Rt} = (10^{13}$–$10^{14})$ $M_\odot$ and $R_t = (10.045$–$100.45)$ kpc, respectively, for $v = 1000$ km s^{-1}. The SMFP core masses and transition radii for modified-core isothermal profile given by Equation (31) are obtained as $M_{\rm Rt} = 10^5$ $M_\odot$ and $R_{\rm t} = (4.55$–$21.57)$ pc, respectively, for $v = 100$ km s^{-1} and $M_{\rm Rt} = 10^5$ $M_\odot$ and $R_{\rm t} = (21.57$–$101.88)$ pc, respectively, for $v = 1000$ km s^{-1}. The accretion radius (10^{-4}–10^{-5}) pc for a 20 $M_\odot$ seed black hole inside an SMFP core is found to be lesser than the transition radius separating the SMFP and LMFP regions. Thus, in the process of collapse, the fluid-like core forms earlier than the termination of accretion. Within the short mean-free path regime ($\lambda < $ H), the black hole densities ($\rho_{\rm BH} = (10^{-13}$–$10^{-10})$ g cm^{-3}) are found to be much larger than the minimum SIDM halo densities ($\rho^* = (10^{-22}$–$10^{-19})$ g cm^{-3}) (see Table 5). For the NFW profile, the SMFP core densities evaluated for different core masses within all the values of halo concentration (7.018, 15.12, 32.58, 4.754, 10.24, and 22.07) and velocity dispersion ($v = 100$ km s^{-1} and 1000 km s^{-1}) are of the order of the minimum SIDM halo density required for a fluid-like behavior. On the other hand, the SMFP core densities calculated for the SIS profile as well other cuspy profiles for the entire range of $\sigma/m_{\rm dm} = (0.1$–$5)$ cm^2 g^{-1} are larger than the corresponding minimum SIDM halo density. The SMFP core densities evaluated for both the modified-core isothermal profiles are also found to be larger than the minimum SIDM halo density (ρ^*). Therefore, the SMFP cores are fluid-like structures, irrespective of the dark matter profile.

For the NFW profile with inner slope of $\beta = 1$, SIS profile, and other cuspy profiles with cusp index in the range (2.19–2.5), the growth timescales of massive black holes (10^3–10^8) $M_\odot$ have been calculated by assuming an initial seed of 20 $M_\odot$ moving with a velocity $v_s = 100$ km s^{-1}. The characteristic overdensity (δ_0) and the scale density (ρ_c) for the NFW profile are evaluated for all values of halo concentration, which are then used for evaluating the timescales of black hole formation. These timescales are displayed in Figure 1 (for halo mass $M_{200} = 10^{12}$ $M_\odot$), Figure 2 (for halo mass $M_{200} = 10^{13}$ $M_\odot$), and Figure 3 (for halo mass $M_{200} = 10^{14}$ $M_\odot$).

The timescales are found to be dependent on the sound speed as well as halo concentration. It is found that the black holes (10^3–10^8) $M_\odot$ grow within (4.77–68.9) Myr for $C = 7.018$, (0.73–10.5) Myr for $C = 15.12$, (0.1–1.45) Myr for $C = 32.58$, (3.65–52.79) Myr for $C = 4.754$, (0.59–8.63) Myr for $C = 10.24$, and (0.86–1.25) Myr for $C = 22.07$. If the process of the formation of these black holes gets started at $z_i = 20$–30, then they are found to be settled at redshifts (z_f) much earlier than quasar epochs (see the arrays attached to Figures 1–3). The growth of these black holes is, therefore, sensitive to the halo concentration and thus, halo mass (M_{200}). Higher halo masses (10^{13} $M_\odot$ and 10^{14} $M_\odot$) allow the formation of massive black holes within few Myr at redshifts quite close to 20. Lower halo mass (10^{12} $M_\odot$) allows black holes to form within few tens of Myr at redshifts $z_f > 15$.

For SIS profiles, the black holes with mass (10^3–10^8) $M_\odot$ grow within (0.33–33.01) Myr. The redshift of formation of these black holes lies very close to $z_f = 20$ or 30 (see Figure 4 and adjacent array). For other power-law profiles ($2.19 \leqslant \gamma \leqslant 2.5$), low-mass black holes (10^3–10^5) $M_\odot$ form within a short period of time, while massive black holes (10^6–10^8) $M_\odot$ grow within few tens to hundreds of Myr (see Figures 5–8). While low-mass black holes form by the epoch very close to z_i, massive black holes form within $z_f =$ (5.05–27.96). Higher values of the cusp index bring the epoch of formation of these black holes to the quasar epoch but with the preference of low-mass black holes (10^3–10^4) $M_\odot$ as the SMFP core masses decrease with the cusp index. Therefore, for these power-law profiles, massive black holes at high redshift are permitted by the lower value of the cusp index.

For the modified-core isothermal profile given by Equation (28), (10^3–10^8) $M_\odot$ black holes form within a short period of time (0.79–23.85) Myr, and hence, they form at epochs very close to z_i (see the arrays attached to Figure 9). For the modified-core isothermal profile given by Equation (31), low-mass black holes (10^3–10^5) $M_\odot$ form within (0.93–30.77) Myr, and 10^6 $M_\odot$ black holes form within 464.08 Myr (see the arrays attached to Figure 10). Massive black holes of mass (10^7–10^8) $M_\odot$ are unable to form within the Hubble time, and hence, they are not shown in Figure 10.

It has been found that, irrespective of the dark matter mass profiles, the massive black holes form well before the quasar epoch. Epochs of formation of these black holes are within $z = 5$–30. Therefore, the SIDM scenario may likely take into account the existence of very massive black holes in the cosmic dawn ($z > 10$). The importance of consideration of low-mass seed black holes (20 $M_\odot$) is to speculate on the maximum time available for a low-mass seed to grow into a massive black hole from dark matter accretion within the different choices of the parameters. Formation of these seeds within a few hundred million years leaves sufficient time for growth into SMBHs.

6. Conclusion

It has been found that within the standard cosmological model, the massive black holes formed well before the epoch accommodating the highest redshift quasars (7.085 recorded by Mortlock et al. 2011 and 7.64 recorded by Wang et al. 2021). Since massive black holes form in the redshift slice $z = 5$–30 (depending upon dark matter distribution), we wish to infer that formation channel seeded by stellar-mass black holes is not a closed case, provided dark matter has self-interaction in the early Universe. Here we also put an important remark about the IMBH-type black holes, i.e., (10^5–10^6) $M_\odot$. This mass scale is also found to be possible in the direct-collapse scenario (Latif et al. 2013). Therefore, SIDM accretion becomes equally eligible for producing heavy black holes for the SMBHs at the high-redshift Universe, irrespective of the mass profile of dark matter. Therefore, the accretion of SIDM provides a serious alternative of existing models of formation of SMBHs. The heavy black holes forming at very high redshift allow sufficient time for development of quasar activity at $z \simeq 7$–8. The generation of very massive black holes (10^7–10^8) $M_\odot$ at $z > 10$ may be a precursor of massive galaxies in the early Universe, thanks to the correlation between the black hole mass and galaxy mass.

The findings reported here are of potential importance for discussion of new dark matter physics in SMBH environments. The fluid-like nature of SIDM core developing into massive black holes found in this work is an important new aspect of dark matter black hole physics. The massive black holes generated can be potential targets for the existing and upcoming terrestrial and space-based gravitational-wave observatories that will be dedicated to study the early black hole population and nature of dark matter. These observations are expected to distinguish between the models of formation of the SMBH.

Acknowledgments

The authors deeply acknowledge Tanushree Bezbaruah of Tezpur University for help in the initial preparation of the manuscript.

Author N.D. would also like to thank Devabrat Sharma of Institute of Advanced Study in Science and Technology, Guwahati for help in some of the computations.

Supporting Data

The data used for the current work will be made available on reasonable request to the corresponding author.

ORCID iDs

Sanjeev Kalita https://orcid.org/0000-0002-2880-4284

References

Arguelles, C. R., Diaz, M. I., Krut, A., et al. 2021, MNRAS, 502, 4227
Balberg, S., & Shapiro, S. L. 2002, PhRvL, 88, 101301
Balberg, S., Shapiro, S. L., & Inagaki, S. 2002, ApJ, 568, 475
Banados, E., Venemans, B. P., Mazzucchelli, C., et al. 2018, Natur, 553, 473
Begelman, M. C., Volonteri, M., & Rees, M. J. 2006, MNRAS, 370, 289
Begeman, K. G., Broelis, A. H., & Sanders, R. H. 1991, MNRAS, 249, 523
Binney, J., & Tremaine, S. 1987, Galactic Dynamics (Princeton, NJ: Princeton Univ. Press)
Blecha, L., Loeb, A., & Narayan, R. 2013, MNRAS, 429, 2594
Bondi, H. 1947, MNRAS, 107, 410
Bondi, H. 1952, MNRAS, 112, 194

Bondi, H., & Hoyle, F. 1944, MNRAS, 104, 273
Bromm, V. 2013, RPPh, 76, 112901
Bromm, V., & Loeb, A. 2003, ApJ, 596, 34
Brownstein, J. R. 2009, PhD thesis, Univ. of Waterloo
Carr, B., & Kuhnel, F. 2020, ARNPS, 70, 355
Cen, R., & Safarzadeh, M. 2015, ApJL, 798, L38
Chan, M. H., Lee, C. M., & Yu, C. W. 2022, NatSR, 12, 15258
Chandrasekhar, S. 1943, ApJ, 97, 255
Choquette, J., Cline, J. M., Cornell, J. M., et al. 2019, JCAP, 2019, 036
Costa, T., Sijacki, D., Trenti, M., et al. 2014, MNRAS, 439, 2146
Cruz, A., Pontzen, A., Volonteri, M., et al. 2021, MNRAS, 500, 2177
Cruz-Osorio, A., Sanchez-Salcedo, F. J., & Lora-Clavijo, F. D. 2017, MNRAS, 471, 3127
De Blok, W. J. G. 2010, AdAst, 2010, 789293
de Blok, W. J. G., McGaugh, S. S., Bosma, A., et al. 2001, ApJL, 552, L23
Di Cintio, A., Tremmel, M., Governato, F., et al. 2017, MNRAS, 469, 2845
Feng, W. X., Yu, H. B., & Zhong, Y. M. 2021, ApJL, 914, L26
Firmani, C., D'Onghia, E., Chincarini, G., et al. 2001, MNRAS, 321, 723
Fields, B. D., Shapiro, S. L., & Shelton, J. 2014, PhRvL, 113, 151302
Giersz, M., Leigh, N., Hypki, A., et al. 2015, MNRAS, 454, 3150
Guzman, F. S., & Lora-Clavijo, F. D. 2011, MNRAS, 416, 3083
Haehnelt, M. G., & Rees, M. J. 1993, MNRAS, 263, 168
Haiman, Z., Rees, M. J., & Loeb, A. 1997, ApJ, 476, 458
Hawking, S. W. 1989, PhRvL, 231, 237
Jimenez, R., Verde, L., & Oh, S. P. 2003, MNRAS, 339, 243
Lalremruati, P. C., & Kalita, S. 2022, ApJ, 941, 183
Larson, L. R., Finkelstein, S. L., Kocevski, D. D., et al. 2023, ApJL, 953, L29
Latif, M. A., Schleicher, D., Schmidt, W., et al. 2013, MNRAS, 436, 2989
Lodato, G., & Natarajan, P. 2006, MNRAS, 371, 1813
Lora-Clavijo, F.D, Guzmán, F.S, & Cruz-Osorio, A 2013, JCAP, 2013, 015
Lynden-Bell, D., & Eggelton, P. P. 1980, MNRAS, 191, 483
Lynden-Bell, D., & Rees, M. J. 1971, MNRAS, 152, 461
Lynden-Bell, D., & Wood, R. 1968, MNRAS, 138, 495
Marel, R. P. V., & Bosch, F. C. V. 1998, AJ, 116, 2220
Markevitch, M., Gonzalez, A. H., Clowe, D., et al. 2004, ApJ, 606, 819
Matsuoka, Y., Iwasawa, K., Onoue, M., et al. 2019, ApJ, 883, 183
McMillan, P. J. 2017, MNRAS, 465, 76
Melia, F., & McClintock, T. M. 2015, RSPSA, 471, 20150449
Mezcua, M., Civano, F., Marchesi, S., et al. 2018, MNRAS, 478, 2576
Misner, C. W. 2023, RNAAS, 7, 142
Mo, H. J., Mao, S., & White, S. D. M. 1998, MNRAS, 295, 319
Moore, B. 1994, Natur, 370, 629
Moore, B., Quinn, T., & Governato, F. 1999, MNRAS, 310, 1147
Mortlock, D. J., Warren, S. J., Venemans, B. P., et al. 2011, Natur, 474, 616
Navarro, J. F., Frenk, C. S., & White, S. D. M. 1996, ApJ, 462, 563
Navarro, J. F., Frenk, C. S., & White, S. D. M. 1997, ApJ, 490, 493
Oh, S. H., Brook, C., Governato, F., et al. 2011, AJ, 142, 24
Ostriker, J. P. 2000, PhRvL, 84, 5258
Pacucci, F., Baldassare, V., Cappelluti, N., et al. 2019, BAAS, 51, 117
Penner, A. J. 2013, MNRAS, 428, 2171
Petterson, J. A. 1978, ApJ, 224, 625
Planck Collaboration, Aghanin, N., Akrami, Y., et al. 2020, A&A, 641, A6
Rees, M. J. 1978, PhyS, 17, 193
Reines, A. E., Greene, J. E., & Geha, M. 2013, ApJ, 775, 116
Reinoso, B., Schleicher, D. R. G., Fellhauer, M., et al. 2018, A&A, 614, A14
Ricarte, A., Tremmel, M., Natarajan, P., et al. 2021, MNRAS, 503, 6098
Rocha, M., Peter, A. H. G., Bullock, J. S., et al. 2013, MNRAS, 430, 81
Salucci, P. 2001, MNRAS, 320, L1
Seth, A. C., Cappellari, M., Neumayer, N., et al. 2010, ApJ, 714, 713
Shimasaku, K., & Izumi, T. 2019, ApJL, 872, L29
Sicilia, A., Lapi, A., Boco, L., et al. 2022, ApJ, 934, 66
Springel, V., Di Matteo, T., & Hernquist, L. 2005, MNRAS, 361, 776
Springel, V., Frenk, C. S., & White, S. D. M. 2006, Natur, 440, 1137
Tulin, S., & Yu, H. B. 2017, PhR, 730, 1
Valluri, M., Ferrarese, L., Merritt, D., et al. 2005, ApJ, 628, 137
Villalba, D. I., Bonoli, S., Dotti, M., et al. 2020, MNRAS, 495, 4681
Vogelsberger, M., Zavala, J., Simpson, C., et al. 2014, MNRAS, 444, 3684
Volonteri, M., Habouzit, M., & Colpi, M. 2021, NatRP, 3, 732
Volonteri, M., & Rees, M. J. 2005, ApJ, 633, 624
Wang, F., Fan, X., Yang, J., et al. 2021, ApJ, 908, 53
Wang, J., Bose, S., Frenk, C. S., et al. 2020, Natur, 585, 39
Wu, X. B., Wang, F., Fan, X., et al. 2015, Natur, 518, 512